



HAL
open science

Irreversible capacity loss of Li-Ion batteries cycled at low temperature due to an untypical layer hindering Li diffusion into graphite electrode

Bramy Pilipili Matadi, Sylvie Geniès, Arnaud Delaille, Claude Chabrol, Eric de Vito, Michel Bardet, Jean-Frederic Martin, Lise Daniel, Yann Bultel

► To cite this version:

Bramy Pilipili Matadi, Sylvie Geniès, Arnaud Delaille, Claude Chabrol, Eric de Vito, et al.. Irreversible capacity loss of Li-Ion batteries cycled at low temperature due to an untypical layer hindering Li diffusion into graphite electrode. *Journal of The Electrochemical Society*, 2017, 164 (12), pp.A2374 - A2389. 10.1149/2.0491712jes . hal-01629474

HAL Id: hal-01629474

<https://hal.science/hal-01629474v1>

Submitted on 5 Sep 2024

HAL is a multi-disciplinary open access archive for the deposit and dissemination of scientific research documents, whether they are published or not. The documents may come from teaching and research institutions in France or abroad, or from public or private research centers.

L'archive ouverte pluridisciplinaire **HAL**, est destinée au dépôt et à la diffusion de documents scientifiques de niveau recherche, publiés ou non, émanant des établissements d'enseignement et de recherche français ou étrangers, des laboratoires publics ou privés.



Distributed under a Creative Commons Attribution 4.0 International License



Irreversible Capacity Loss of Li-Ion Batteries Cycled at Low Temperature Due to an Untypical Layer Hindering Li Diffusion into Graphite Electrode

Bramy Pilipili Matadi,^{a,b} Sylvie Geniès,^{b,c} Arnaud Delaille,^{a,b,z} Claude Chabrol,^{b,c} Eric de Vito,^b Michel Bardet,^d Jean-Frédéric Martin,^{b,c} Lise Daniel,^{b,c} and Yann Bultel^{e,f}

^aUniv. Grenoble Alpes, INES, F-73375 Le Bourget du Lac, France

^bCEA, LITEN, F-38054 Grenoble, France

^cUniv. Grenoble Alpes, F-38000 Grenoble, France

^dCEA, DRF/INAC, MEM, RM, F-38054 Grenoble, France

^eUniv. Grenoble Alpes, LEPMI, F-38000 Grenoble, France

^fCNRS, LEPMI, F-38000 Grenoble, France

This paper deals with the occurrence of a graphite irreversible degradation mechanism in commercial Graphite (C) / lithium Nickel Manganese Cobalt oxide (NMC) lithium-ion batteries, challenging metallic lithium deposition as the major aging mechanism at low temperature cycling. In this study, commercial 16 Ah C/NMC Li-ion cells were aged during cycling at 5°C at a rate of 1C between 2.7 V and 4.2 V (namely between 0 and 100% of state of charge (SOC), respectively), with significant performance fading after 50 cycles only, while up to 4000 cycles can be performed at 45°C with the same commercial cells. The monitoring of the potential of each electrode during cycling has been performed through the successful introduction of lithium metal as reference electrode into the commercial cell. This technique demonstrated that it was more and more difficult to extract lithium ions from graphite particles to intercalate into the positive electrode as the number of cycles increased. Graphite electrodes remained unexpectedly lithiated after cells were dismantled in discharged state. A part of exchangeable lithium detected being trapped into the negative electrode as graphite intercalation compounds was observed with X-Ray Diffraction (XRD). Lithium-7 Nuclear Magnetic Resonance (⁷Li NMR) performed on graphite electrode led to the distinction between lithium intercalated into graphite, oxidized lithium in the Solid Electrolyte Interphase (SEI) and metallic lithium present in low amounts. Coupling Focused Ion Beam (FIB) / Time-of-Flight Secondary Ion Mass Spectrometry (ToF-SIMS) and Photoelectron Spectrometry (XPS) techniques demonstrated the presence of an untypical layer composed of electrolyte degradation products, hindering graphite electrode pores, particularly concentrated in the regions corresponding to interparticle cavities where lithium was found enriched and trapped.

© The Author(s) 2017. Published by ECS. This is an open access article distributed under the terms of the Creative Commons Attribution 4.0 License (CC BY, <http://creativecommons.org/licenses/by/4.0/>), which permits unrestricted reuse of the work in any medium, provided the original work is properly cited. [DOI: 10.1149/2.0491712jes] All rights reserved.



Manuscript submitted June 19, 2017; revised manuscript received July 28, 2017. Published August 10, 2017. This was Paper 927 presented at the Honolulu, Hawaii, Meeting of the Society, October 2–7, 2016.

Lithium-ion batteries address applications as diverse as mobile electronic devices, electric vehicles or stand-alone energy storage systems. The aging of lithium-ion batteries is largely studied and can be related to complex inter-dependencies from intrinsic cell components on one hand (electrodes materials, electrolyte composition^{1–10}) and from extrinsic criteria on the other hand (temperature, applied charge/discharge current-rate, charge/discharge cutoff voltages, depth of charge/discharge, cell design^{11–14}).

In applications such as marine, aeronautics, military space and other systems under severe conditions, batteries can be used sometimes at low temperature, typically below 10°C. In such conditions, it is well known that the performance of Li-ion batteries is reduced in most of the cases, the kinetics of lithium intercalation-deintercalation being affected due to the limited mobility of lithium cations in the electrolyte.¹⁵ Moreover, C.-K. Huang et al. suggested that the poor low-temperature performance of Li-ion cells is exclusively related to the reduced Li diffusivity in carbon electrodes and not organic electrolytes neither SEI.¹⁶

Graphite is one of the most common materials used as negative electrode in lithium-ion batteries. It stores lithium at a range of 0.05 V vs. Li⁺/Li - 0.1 V vs. Li⁺/Li.^{17–20} Be that as it may, charging at low temperatures increases internal resistance which can lower the potential of graphite below 0 V vs. Li⁺/Li, hence lithium metal deposition on the anode surface, known as lithium plating, is facilitated.²¹ We can also notice that due to the overpotential associated with charging at low temperatures, the anode potential may have to be well below 0 V vs. Li⁺/Li prior to lithium plating occurring, depending upon the charge rate. Lithium deposition on the carbon anode is due to low lithium cation diffusion in the anode and/or across the SEI.²² In the literature, lithium plating is reported to be the main cause of lithium-ion batteries aging at low temperature and/or at high charge rate.^{23–32}

Lithium carbonate compounds can be formed in case of contact between the metallic lithium and the electrolyte on the surface of the SEI. On the whole, the loss of the exchangeable lithium leads to an irreversible loss of the capacity of the lithium-ion battery.

In the literature, methods for physical and chemical characterization of aged battery materials have been recently reviewed by T. Waldmann et al.³³ It is possible to detect depositions on the electrode surface in the μm size range using optical microscopy methods. S.J. Harris et al. described in situ measurements of Li transport in an operating cell using an Olympus SZX12 optical microscope in order to study the graphite lithiation and coloration process, Li plating and Li dendrite growth.³⁴ C. Uhlmann et al. observed the growth and relaxation of macroscopically plated lithium using an optical confocal microscopy whilst applying current.³⁵ J. Steiger et al. used a light microscope to observe the modification of the SEI at crystalline defects and the dissolution of electrodeposited lithium filaments.³⁶ In situ optical investigations to analyze lithium metal plating have also been performed by other authors such as O. Crowther et al.³⁷ and H. Wu et al.³⁸ However, the detection of particle cracks is limited by the resolution of optical microscopes which corresponds to a range of 0.2 μm.³⁹

The growth of the SEI⁴⁰ or the morphology of Li deposition (dendritic, granular or foamy)⁴¹ on the surface of graphite particles can also be observed with images obtained from Scanning Electron Microscopy (SEM). This method is often completed with Focused Ion Beam (FIB) technique for 3D visualizations. In addition to SEM, structural changes of electrodes materials after aging can be investigated with Transmission Electron Microscopy (TEM) analysis.

Energy Dispersive X-ray spectroscopy (EDX) and X-ray Photoelectron Spectroscopy (XPS) are used in order to determine the chemical composition of the analyzed area. XPS can be combined with ion sputtering to obtain depth profiles useful to investigate the SEI layer.⁴² F. German et al. reported that with the combination of XPS

^zE-mail: arnaud.delaille@cea.fr

Table I. Protocol of cycling at 5°C according to the following voltage limits strategies. The capacity of each Li-ion cell is measured at the beginning of life (BOL) and at the end of life (EOL) at a rate of 1C at 25°C.

Cells	Voltage limits (V)	Charge with CV	Full Equivalent Cycles	Capacity @25°C (Ah)		Loss of capacity (%)	Status
				BOL	EOL		
1	2.70 - 4.20	No	38	17.30	3.49	79.83	Backup
2	2.70 - 4.20	Yes	50	16.96	4.01	76.36	Swollen
3	2.70 - 4.20	Yes	50	17.24	4.84	71.93	Post-Mortem
4	2.70 - 4.20	Yes	50	17.18	4.24	75.32	Instrumented Ante-Mortem
5	3.42 - 4.08	Yes	1509	17.27	15.20	11.99	Post-Mortem

and Fourier Transform Infrared Spectroscopy (FTIR) measurements it was possible to identify the constituents of the outer and inner SEI.⁴³ Further investigations of graphite electrodes can be achieved with Glow Discharge Optical Emission Spectroscopy (GD-OES). N. Ghanbari et al. used this technique to determine significant differences between anodes with Li deposition and with SEI.⁴⁴

Another chemical analysis method sensitive to electrode surfaces such as Time-of-Flight Secondary Ion Mass Spectrometry (ToF-SIMS) and chemical analysis methods for electrode bulk analysis such as Nuclear Magnetic Resonance (NMR) as well as X-Ray Diffraction (XRD) will be described in detail in this paper in the following sections.

In addition to required post-mortem analyses, the detection of metallic lithium deposition is possible by measuring the potential of the negative electrode using a reference electrode. Such measurements are possible using a reconstruction of both negative and positive electrodes recovered from a commercial cell into a three-electrodes full cell with an additional reference electrode such as metallic lithium.⁴⁵⁻⁴⁷ However, measurements obtained from a reconstructed lithium-ion cell may be influenced by several factors: the necessity of removing one of the two faces of each electrode recovered from the commercial cell, the protocol of washing electrodes, the nature of the electrolyte which may be different from the original one used in the commercial cell. Besides, the assembly of reconstructed 3-electrode full cells is performed in an anhydrous room. The exposure of electrodes, especially graphite, to the atmosphere of the anhydrous room has a negative impact on electrochemical impedance spectroscopy curves. The reconstructed 3-electrodes full cell has a higher resistance than the original cell at the end of discharge/charge. T. Waldmann et al.²⁰ reported that the reason for that difference is due to the different heating behavior between commercial and reconstructed 3-electrode cells during charging.

Nevertheless, rigorous measurements can be obtained with a reference electrode directly inserted into the commercial battery by allowing the tracking of the evolution of the potential of each electrode with aging. Necessary expertise has been required to address this challenge.

This paper presents the study of a degradation mechanism of graphite electrodes. Commercial 16 Ah C/NMC Li-ion batteries are aged during cycling at 5°C at a rate of 1 C resulting in a considerable irreversible loss of capacity in 50 cycles. In fact, the State of Health (SOH) is around 25% after cycling and the capacity is not recovered at low current. Ante-mortem analyses consisting in the investigation with a reference electrode directly inserted into a commercial cell are performed in order to follow up the potential of each electrode during cycling. Results obtained from post-mortem investigations in agreement with ante-mortem experiments put into evidence that a lithium trapping mechanism into graphite electrode with pores hindered by a layer composed of electrolyte degradation products seems to be the main cause of the capacity fade observed.

Experimental

Electrochemical characterization.—*Considered Li-ion cell.*—Commercial high power lithium-ion polymer pouch cells with a nominal capacity of 16 Ah and an energy density of 146 Wh/kg have been

used. A voltage range of 2.7–4.2 V is allowed. Graphite is the negative electrode and NMC oxide is the positive electrode while the separator is constituted by microporous polyethylene film and the electrolyte is based on carbonates.

Protocol of cycling tests.—In the datasheet of the manufacturer, it is recommended to not charge this commercial Li-ion cell over 0.3 C in a temperature range of 0 ~ 10°C while no current limitation is indicated for the discharging rate in the same range of temperature. Nevertheless, it has been decided to apply a rate of 1C both in charge as in discharge in order to study associated aging mechanisms under these conditions.

Five cells are thus considered for cycling tests performed at 5°C at a rate of 1 C in charge as in discharge following the protocol of voltage limits described in Table I. For some cells, the charge ends with a constant voltage (CV) phase which starts when the cutoff voltage is reached and stops when the current drops to C/20. Full depth-of-discharge, namely cycling between 2.7 - 4.2 V (voltage thresholds corresponding to 0 - 100% SOC) is applied on the four first cells, while another profile has been performed on a fifth cell consisting in cycling between 3.42 - 4.08 V (voltage thresholds corresponding to 10% SOC - 90% SOC) with again a CV phase during the charge when the upper-bound voltage limit is reached. The correspondence between the end-of-voltage windows and the SOC limits were determined from voltage curves measured at the beginning of life at 25°C. Note that the correspondence between SOC limits and voltage thresholds may be different at other temperatures or C-rates and may also evolve with aging. Consequently these voltage ranges do not correspond rigorously to specified SOC ranges for other temperatures, C-rates, or after aging. Finally, one commercial cell is instrumented with a reference electrode based on lithium metal. The reference capacity of each cell is measured in discharge at 25°C at a rate of 1 C with a CV phase at the beginning of life (BOL) and after the cycling period.

Introduction of a reference electrode into a commercial cell.—The electrochemical couple constituting the reference electrode must present a plateau of potential on a wide range of state of charge and be stable in the electrolyte. The major difficulty is to have a stable potential over time in order to make reliable long-term characterizations during cycling tests. In lithium-ion cells, different redox couples are also used as a reference electrode. The most commonly used material is metallic lithium: Li⁺/Li ($U_{\text{plateau}} = 0$ V vs. Li⁺/Li). Note that the value of the potential of negative electrode vs. Li⁺/Li can be used as an indicator of metallic lithium deposition on graphite electrode. The aim is to follow up the evolution of the potential of each electrode vs. Li⁺/Li subjected to alternated charge /discharge profiles during cycling in order to understand aging mechanisms involved. The Figure 1 presents the insertion of a reference electrode into a fresh 16 Ah commercial Li-ion battery performed in discharged state in the Argon-filled glove. A lithium metal electrode of a surface of 16 mm² and a thickness of 50 μm is used as reference electrode. Before being inserted into the cell, lithium metal is then protected by a separator film soaked by the electrolyte. The reference electrode is attached on a copper grid. The presence of the copper grid prevents the formation of inductive loops in electrochemical impedance spec-

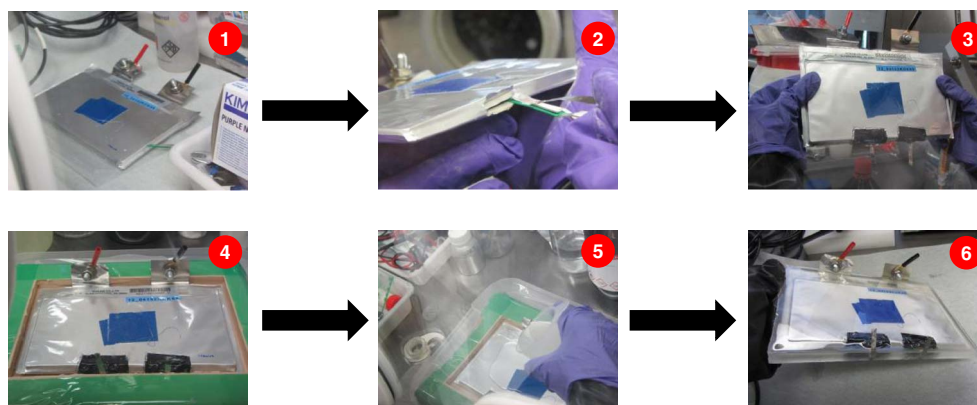


Figure 1. Procedure of the insertion of metal lithium as reference electrode into a 16 Ah commercial Li-ion cell. (1): Illustration of the fresh 16 Ah commercial high power Li-ion pouch cell. (2): A lithium metal electrode of a surface of 16 mm² and a thickness of 50 μm is inserted into the cell. Ni is used as the current collector. (3): Once the reference electrode is introduced into the battery, external incisions are done for isolation. The second reference electrode serves as a backup. (4): The cell is placed in a mold before being resined. (5): The instrumented cell is then completely resined for safety reasons. (6): 16 Ah commercial Li-ion pouch cell instrumented with reference electrodes.

troscopy measurements. Ni is used as the current collector. Once the reference electrode is introduced into the battery, external incisions are isolated. Prior to perform cycling test with this instrumented cell, electrochemical impedance spectroscopy measurements and electrochemical characterizations were performed respectively at 25°C, 45°C and 5°C and at different C-rates in order to verify that cell integrity is not compromised by the insertion of a reference electrode. As a result, no derivation of the performance of the instrumented cell, neither of the reference electrode behavior were observed during these preliminary tests.

Cell dismantling and sample preparation.—Before dismantling, cells are discharged at a rate of C/10 until the minimum voltage of 2.7 V. The same discharge procedure is repeated once after a rest of 5 minutes. Cells are disassembled in an Argon-filled glove box using a ceramic knife. These commercial 16 Ah Li-ion cells contain 23 bifacial and 2 single-facial positive electrodes and 24 bifacial negative electrodes. The electrode pairs in the middle of the pouch cells are considered for analysis. Numeric pictures of both electrodes and separators are taken for visual inspections. Graphite samples are then brought to a SEM equipment with a transfer chamber, used to avoid exposure to the air, for surface analysis. The electrolyte samples are retrieved very quickly during the dismantling of cells inside the Argon-filled glove box by immersing a slice of separator in CH₃CN used as a carrier solvent for at least 2 hours. The solution is then transported to the Gas Chromatography – Mass Spectrometry (GC-MS) split / splitless injector without air exposure in order to determine the composition of the electrolyte.

Electrochemical measurements of single components.—N-Methyl-2-pyrrolidone (NMP) is used to remove the coating of one side from electrodes extracted from commercial cells. Single components are then assembled in different types of laboratory coin cells under argon atmosphere for electrochemical characterizations.

Coin half cells.—They consist of graphite-based electrode or NMC-based electrode (16 mm) from the commercial cell and Celgard 2400 separator (18 mm) with a metal lithium electrode in 1:1:1 wt EC:DMC:EMC + 1 M LiPF₆ electrolyte. The capacity of lithium de/re-Intercalation into both graphite and NMC electrodes recovered from aged cells is investigated with coin half-cells.

Three CR2032 Graphite/Li metal coin half-cells (A, B and C) are assembled as presented in Table II. The nominal capacity of each coin half-cell is 3.3 mAh with $V_{\min} = 0.02$ V and $V_{\max} = 1.5$ V. The first Graphite/Li metal coin half-cell (A) is based on a fresh graphite electrode while the two others (B and C) contain graphite samples recovered from aged commercial cells. In parallel, two CR2032 NMC/Li metal coin half-cells (D and E), based on a fresh (D) and an aged (E) NMC electrode respectively, are assembled (see in Table II). The nominal capacity of each NMC/Li metal coin half-cell is 2.88 mAh with $V_{\min} = 2.6$ V and $V_{\max} = 4.1$ V.

Electrochemical characterizations are performed at 25°C, at different C-rates according to the following order: 0.1C, 0.2C, 0.5C, 1C, 2C, 5C, 8C, 0.2C and 0.1C at least. Charges at 0.1C are performed with a CV phase until the current reaches C/50. Between charge and discharge, a rest of 30 minutes is programmed for Graphite/Li metal coin half-cells and 5 minutes for NMC/Li metal coin half-cells. Each

Table II. Post-mortem electrochemical measurements (performed at 25°C) of single components with coin half cells. The nominal capacity of each Graphite/Li metal coin half-cell is 3.3 mAh with $V_{\min} = 0.02$ V and $V_{\max} = 1.5$ V while the nominal capacity of each NMC/Li metal coin half-cell is 2.88 mAh with $V_{\min} = 2.6$ V and $V_{\max} = 4.1$ V. The capacity shown in this Table is measured at 0.1 C.

		Graphite / Li metal	
		Capacity measured (mAh)	
		1 st charge	1 st discharge
Graphite from the fresh cell	coin half-cell A	0	2.602
Graphite from the aged cell (cell #3)	coin half-cell B	0.153	1.360
	coin half-cell C	0.202	1.475
		NMC / Li metal	
		Capacity measured (mAh)	
		1 st discharge	1 st charge
NMC from the fresh cell	coin half-cell D	0	2.411
NMC from the aged cell (cell #3)	coin half-cell E	2.289	2.478

Table III. Composition of different electrolytes based on elements detected from the fresh electrolyte with GC-MS: ethyl methyl carbonate (EMC); ethylene carbonate (EC); biphenyl (BP); 1,3 propane sultone (PS); vinylene carbonate (VC), fluoroethylene carbonate (FEC).

Electrolyte	Solvents	Additives
E1	1:1 EMC:EC + LiPF ₆ 1M	BP + PS + FEC + VC
E2		BP + PS + FEC
E3		BP + PS
E4		BP
E5		PS
E6	1:1:1 EMC:EC:DMC + LiPF ₆ 1M	

C-rate is repeated 5 times except the first C-rate at 0.1C which is repeated only 3 times.

It should be noted that the charge process of the Graphite/Li metal coin half-cells corresponds to delithiation process in graphite electrode, since graphite operates as the cathode in this configuration.

Coin full cells.— They consist of graphite-based electrode (16 mm), NMC-based electrode (14 mm) both from the commercial cell and Celgard 2400 separator with six different types of electrolyte based on solvents and additives detected with GC-MS. The influence of the electrolyte composition is investigated with coin full cells.

Twelve CR2032 Graphite/NMC coin full cells are assembled: two coin full cells per type of electrolyte (see in Table III) in order to verify the reproducibility. The nominal capacity of each coin full cell is 2.88 mAh with $V_{\min} = 2.7$ V and $V_{\max} = 4.2$ V. Cycling tests between 2.7–4.2 V are performed at a rate of 1 C with a CV phase in charge. As with 16 Ah commercial pouch-cells, the reference capacity of each coin full cell is measured at 25°C at the beginning of life (BOL) and after the cycling period. After cycling, all the coin full cells are dismantled at a discharged state as it was the case for 16 Ah commercial pouch-cells.

Physico-chemical characterization.—*Structure and lithiation state investigations with XRD.*—XRD measurements are performed in order to verify the structure and the state of lithiation of both graphite and NMC electrodes before and after cycling. Not washed samples ($\Theta = 14$ mm) are recovered from electrodes and protected by a dried Kapton film. X-ray diffractograms are recorded with a BRÜKER D8 Advance apparatus using Cu K α radiation. In situ XRD analysis is also performed on the fresh NMC electrode to create a “calibration” curve that links lattice parameters with SOC values. So, the Li rate of the aged cathodes can be estimated using the lattice parameters of the structure after cycling. For this experiment, powder of NMC is recovered by scratching the fresh electrode. It is cycled against Li in conventional liquid electrolyte in situ XRD cell connected to a VSP Bio-Logic EC Lab cyler unit. The cycling protocol consists in an alternation of 2 steps: a 2 hours step of cycling at C/20 and 4 hours of relaxation. An X-Ray diffractogram is acquired during the last 3 hours of each relaxation step. This is repeated until the end of charge at 4.3 V vs. Li and the end of discharge at 2.6 V vs. Li.

Metallic lithium detection with ⁷Li NMR.—Lithium-7 Nuclear Magnetic Resonance (NMR) technique is used to detect the presence or not of metallic lithium on graphite electrodes. Solid-state MAS NMR measurements were performed on a Bruker AVANCE DSX 200 MHz spectrometer (4.7 T, ⁷Li Larmor frequency $\nu_0 = 77.78$ MHz) equipped with a 1.3 mm Bruker CPMAS probe head. The ⁷Li MAS NMR spectra were recorded at different MAS spinning frequencies in the range 36–60 kHz with direct ⁷Li excitation. Different repetition delays for transient accumulation were tested in the range of 1 to 30 s in order to obtain quantitative data. A ⁷Li 90°-pulse width of 2.2 μ s was used, corresponding to the nucleus magnetization turn angle of about 75–80°. High power proton decoupling was also used but did not improve the quality of the spectra since proton and lithium are not directly linked neither through bond nor through space interactions. All spectra were acquired with room temperature bearing

air, corresponding to a sample temperature in the range of 50–70°C. Aqueous LiCl solution was used as a chemical shift reference set to 0 ppm. A sample of Lithium metal was recorded in order to measure its chemical shift (265 ppm). For illustration of ionic Lithium, a sample of Li₃PO₄ was also recorded.

Graphite depth investigations with FIB/ToF-SIMS.—Chemical investigation has been performed with Time-of-Flight Secondary Ion Mass Spectrometry (ToF-SIMS) combined with in situ Focused Ion Beam (FIB), as successfully used in a previous work.⁴⁸ Here the aim was to analyze in depth graphite electrode samples recovered from aged commercial cells. A FIB wall was achieved at the surface of graphite by Focused Ion Beam (FIB) technique in order to analyze the electrodes in depth. Analyses were essentially performed in negative polarity mode because most of elements (Carbon, Phosphorus, Fluorine, Oxygen), are more sensitive to “negative” ionization except for the lithium which is however relatively well detected.

In order to extract maximum information from FIB-SIMS analysis, a data processing protocol for images is proposed. The raw image corresponding to the substrate (addition of signals C/C₂/C₃ and so on) is retained. The carbon may come from the SEI layer but especially from graphite particles, in particular the fragments C₂/C₃ and so on. For elements in smaller quantities (Li, F, P, O), in connection with SEI, the corresponding images are normalized with respect to the “graphite” image. This minimizes contrast related to topology. In some areas of the ionic images, for various reasons (topography, matrix effects), the intensity of the signal is more important. This means that in these areas, overall, more fragments of atomic / molecular are extracted and therefore the small quantity elements signals are important too. Standardization can confirm which signals are characteristic of the total ionic signal in this area and not due to the overall increase thereof. Moreover, ToF-SIMS investigation is not quantitative. Generated images must be restricted by two threshold values. It is thus proposed to use the same threshold values for a given element and for different experiments. This allows to compare the relative enrichment of the elements according to different electrodes. The maps were obtained with the following resolution: 256 × 256 pixels with 10 shots F; pixel.

Extensive chemical investigations with XPS.—Extensive chemical investigation are conducted with X-Ray Photoelectron Spectroscopy (XPS). The objective of this study is to confirm the interpretation of the FIB-SIMS results. To do this, XPS spectroscopic analysis of the surface of graphite electrodes from aged cells are carried out on a PHI Versaprobe II spectrometer. Spectroscopic and profilometric analyses of the SEI layer are performed with the following parameters: take-off angle = 45°, pass energy = 23.5 eV.

Results and Discussion

State of health of commercial cells.—Figure 2 presents the evolution of the capacity of each 16 Ah Li-ion cell during cycling at 5°C. A considerable loss of performance is observed during the first 50 cycles for the all 4 cells cycled between 2.7 V and 4.2 V. This unexpected capacity fade is also observed with the commercial Li-ion cell instrumented with a reference electrode. Table I shows that the irreversible loss of capacity measured at 25°C is on average about 75% for all the first four cells. These results reflect a good reproducibility. There is no real influence of the CV phase in charge. The condition of cycling between 3.42 V and 4.08 V (cell #5) involves a capacity loss limited to 10% after the same number of cycles. Furthermore, this capacity fade stabilized quickly, and as a result, it has been possible to extend the number of cycles up to 1509 Full Equivalent Cycles (FEC) without any important additional capacity loss defect, about 12% before dismantling. So, for the same conditions of temperature, there is a considerable difference in loss of performance due to the end-of-voltage limits.

After cycling, the cell #1 has been stored as backup in a climate chamber at 12°C while the cell #2 has swollen itself few days after

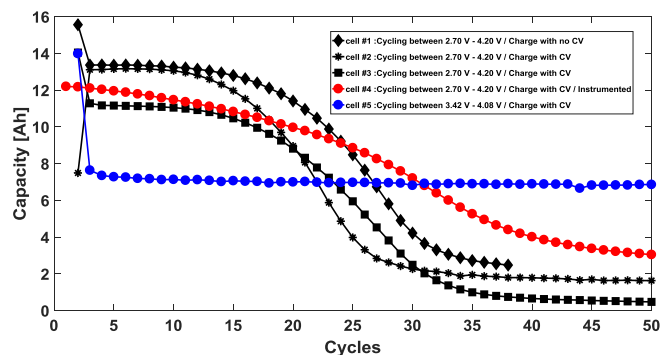


Figure 2. Evolution of the capacity during the cycling test performed at 5°C. Fast loss of capacity is observed for all the Li-ion cells for which cycling tests are performed between 2.7 V and 4.2 V.

inside the same climate chamber. Post-mortem investigations were then investigated with the cell #3 and the cell #5 while ante-mortem analyses were performed with the commercial Li-ion battery instrumented with a reference electrode (cell #4).

Figure 3 shows that the potential of the negative electrode in cell #4 only goes below 0 V vs. Li⁺/Li over the last 6 cycles at the end of the CC phase meanwhile it remains higher than 0 V during the CV phase. Regarding this latter result, the risk of lithium deposition seems to be unlikely in such conditions. However, this assumption will be verified with post-mortem analyses. The detection of metallic lithium depositions with ⁷Li NMR is well discussed in the Detection of metallic lithium with ⁷Li NMR section.

On one hand, the end-of-charge potential (CV phase) of the negative electrode decreases from 62.57 mV vs. Li⁺/Li (1st cycle) to 7.784 mV vs. Li⁺/Li (50th cycle) as a decrease of about 55 mV as shown

in Figure 3. As a result, the end-of-charge potential of the positive electrode drops from 4.254 V vs. Li⁺/Li (1st cycle) to 4.198 V vs. Li⁺/Li (50th cycle). This latter phenomena could be interpreted by the fact that graphite is more and more lithiated at the end of the charge and NMC is less and less lithiated during cycling.

On the other hand, the end-of-discharge potential of the positive electrode is increasingly high as the number of cycles increases as shown in Figure 3. It rises from 3.557 V vs. Li⁺/Li (1st cycle) to 3.872 V vs. Li⁺/Li (50th cycle). It seems that NMC is less and less lithiated. In the same time, the end-of-discharge potential of the negative electrode increases from 0.8583 V vs. Li⁺/Li (1st cycle) to 1.177 V vs. Li⁺/Li (50th cycle), representing an increase of 0.319 V. We can hence do the assumption that it is more and more difficult to extract lithium ions from graphite particles to intercalate into the positive electrode. This mechanism will be thoroughly investigated with post-mortem analysis.

Visual inspections.—A fresh 16 Ah Li-ion cell, cell #3 (cycling between 2.7 V–4.2 V) and cell #5 (cycling between 3.42 V–4.08 V) (as described in Table 1) were disassembled in discharged state for investigations of aging mechanisms involved. Visual inspections of both negative and positive electrodes and separators are presented in Figure 4. No notable degradation is observed on both NMC electrodes. Separators from both cells are still white. Contrary to expectations, no lithium plating is visually observed on the surface of the graphite electrodes. Nevertheless, as the cell was dismantled at a discharged state, lithium plating would be stripped from the surface during discharge as it is well accepted that the lithium plating and stripping phenomenon is largely reversible.

In the literature, some authors reported that metallic lithium deposited on the surface of the graphite electrode can diffuse into the active material during the relaxation time by chemical reaction to form graphite intercalation compounds resulting in a capacity

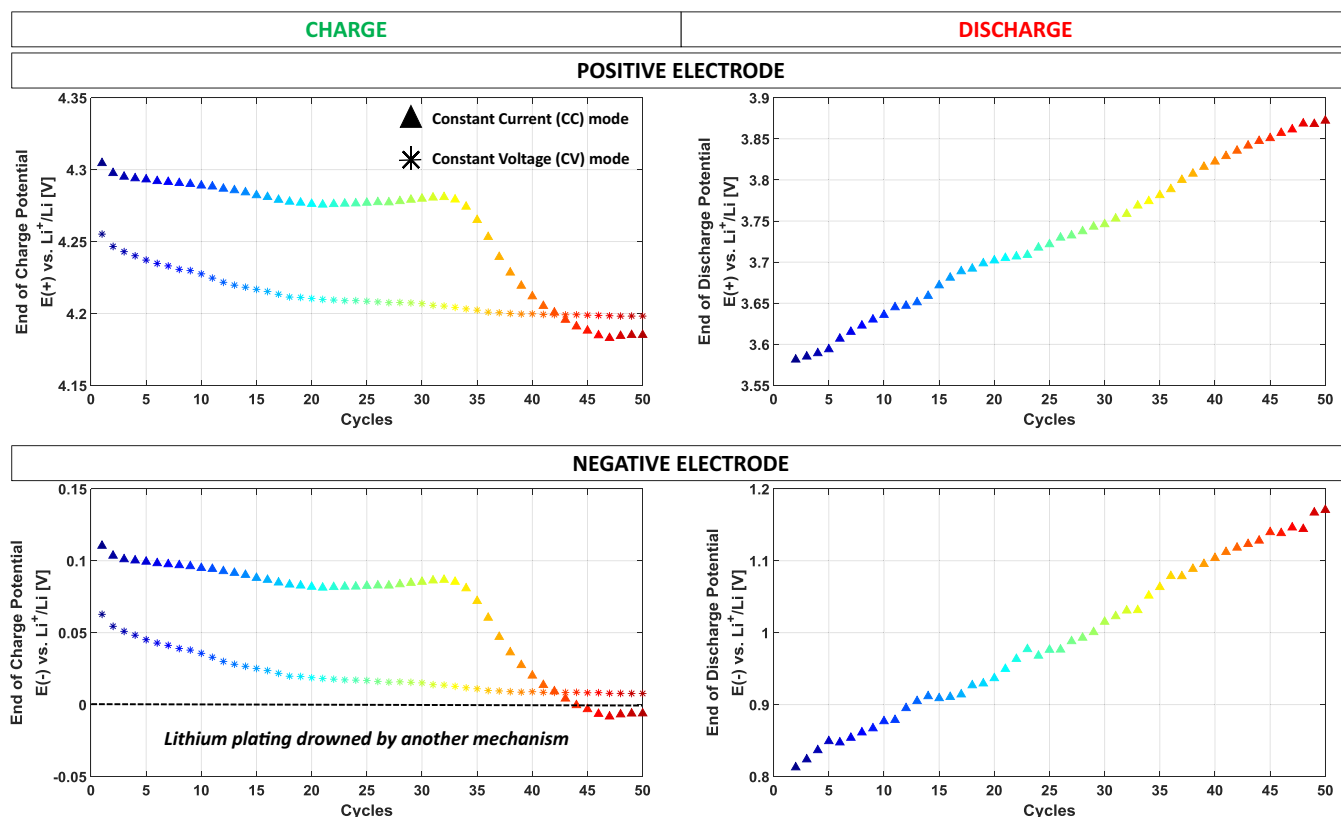


Figure 3. Evolution of the end-of-charge and discharge potentials of both electrodes during cycling at 5°C between 2.7 V and 4.2 V. Measurements obtained with reference electrode inserted in 16 Ah Li-ion cell #4.







Cycling aging at T=5°C and at 1 C	Components			Comments
	NMC	Separator	Graphite	
<p>Cell n°3</p> <p>$U_{\min}=2.70V$ $U_{\max}=4.20V$</p> <p>38 FEC</p> <p>SOH = 22%</p> <p>Duration = 3 days</p>				No Lithium deposition
<p>Cell n°5</p> <p>$U_{\min}=3.42V$ $U_{\max}=4.08V$</p> <p>1509 FEC</p> <p>SOH = 88%</p> <p>Duration = 328 days</p>				No Lithium deposition

Figure 4. Visual inspections at discharged state of both negative and positive electrodes and separators of 16 Ah C/NMC commercial Li-ion pouch cells after cycling at 5°C and at a rate of 1 C.

recovery. J. Fan et al.⁴⁹ suggested that the lithium deposited on the negative surface during the low-temperature charging of a commercial graphite/LiCoO₂ Li-ion cell can rapidly diffuse into graphite during the room temperature rest, while it cannot diffuse during 4 hours rest at -20°C. Paradoxically, V. Zinth et al.⁵⁰ observed, after few cycles performed at -20°C and at a rate of C/30 and C/5, the plated lithium diffusion into graphite in commercial graphite/LiNi_{1/3}Mn_{1/3}Co_{1/3}O₂ cells during a 20 hours rest period at -20°C by in situ neutron diffraction investigations. The authors evoked the diffusion of metallic lithium leading to an ongoing transformation to LiC₁₂ and LiC₆ with a capacity recovery estimated to 17%. Recently, T. Waldmann et al.⁵¹ discussed the chemical intercalation of Li plating into adjacent graphite particles during a rest period at 25°C resulting also in a partly capacity recovery.

By contrast, in our case, after the last check-up, cells, stored at 12°C during two weeks before dismantling, do not show any capacity recovery. So, a potential diffusion of plated lithium into graphite electrodes during rest time resulting in a capacity recovery cannot be evoked.

On one hand, the graphite electrode recovered from the cell #5 presents a black color with no visible defect detected on the surface. On the other hand, the graphite electrode taken from the cell #3 seems rather presenting a lithiated state due to the brown color⁵²⁻⁵⁵ on the surface although the cell was dismantling in discharged state. This observation is reproducible on all the 24 bifacial negative electrodes. Additional post-mortem analyses have been performed for investigating this unexpected mechanism.

Surface morphology and chemical analysis with SEM-EDS.—Figure 5 shows SEM images of graphite electrodes recovered from a fresh commercial Li-ion cell and from the cell #3. The unaged graphite sample presents a normal graphite material appearance, with a crushing aspect on its surface, certainly due to the calendaring effect during industrial manufacturing. The graphite sample of the aged cell presents visually an unexpected brown color (see in Figure 4) attributed to a

lithiated state and particles on the surface looking like “sticks”. The appearance of these “filaments” is quite similar to Li deposition in dendritic morphologies as observed by H. Honbo et al.⁵⁶

Table IV presents the percentage of each element detected with Energy-dispersive X-ray spectroscopy (EDS) that confirms that there is no contamination by elements originating from the positive electrode. Lithium element could not be detected. However, due to its low atomic mass and its low energy of characteristic radiation, lithium element is not detectable with EDS.

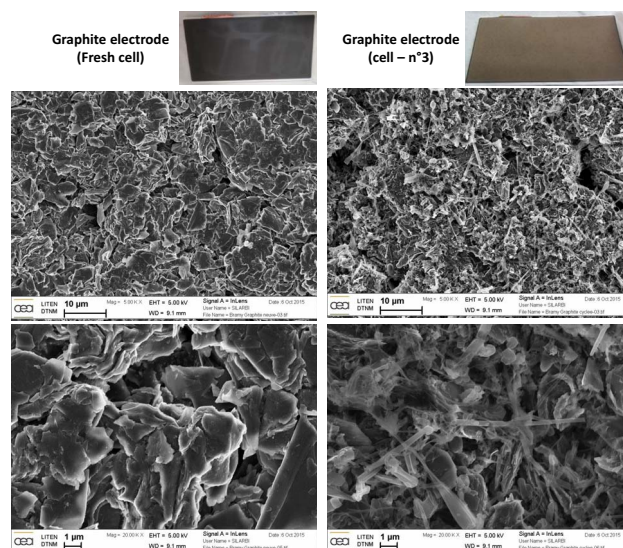


Figure 5. SEM analysis performed on a sample of graphite electrode recovered from the fresh commercial cell and on a sample graphite electrode from the cell #3, after cycling between 2.7 V and 4.2 V.

Table IV. Percentage of each element detected with SEM/EDS on samples of graphite electrodes respectively recovered from a fresh cell and from the cell #3. There is no contamination by elements of the positive electrode.

Element		C	O	F	P	S	Cu
% at.	Fresh cell	82.78	7.69	9.17	0.23	0.12	0
	Cell #3	73.53	16.48	8.87	0.55	0.57	0

State of health of each electrode.—*Electrochemical measurements of single components with coin half cells.*—As it seems difficult to extract more lithium ions from the graphite electrode to intercalate to the positive electrode, we aim to study de/re-intercalation mechanisms. Harvested cells are useful to test if it is still possible to delithiate or to relithiate aged electrodes. NMC/Li metal and Graphite/Li metal coin half cells based on electrodes respectively recovered from a fresh Li-ion cell and from the cell #3 are assembled.

The NMC/Li metal coin half cells are first submitted to a discharge step while the Graphite/Li metal coin half cells are submitted to a charge step performed at a rate of 0.1 C, which is a low C-rate. The aim is to delithiate those electrodes so that the residual capacity of each of the respective electrodes, after dismantling of the cell, can be determined. Thereafter, the capacity of these coin half cells is also measured at other different C-rates as described in the Experimental section.

As presented in Figure 6 and in Table II, the first discharged and charged capacities are respectively 0 mAh and 2.411 mAh for NMC/Li metal coin half-cell based on fresh electrode (D). This result confirms

that the fresh NMC electrode was fully lithiated before dismantling. For the NMC/Li metal coin half-cell based on aged electrode (E), the first discharged and charged capacities are respectively 2.289 mAh and 2.478 mAh. This electrode was therefore not fully lithiated during the last discharge before dismantling. Lithium remained into graphite electrode. In any case, this aged positive electrode exhibits good cycling when further cycled vs. Li metal. No loss of capacity of lithium intercalation with this electrode is observed.

On one hand, the first charged and discharged capacities are respectively 0 mAh and 2.602 mAh for the Graphite/Li metal coin half-cell based on fresh electrode (A). It is a confirmation that the fresh graphite was fully delithiated. It is not possible at all to more delithiate. On the other hand, the first charged and discharged capacities are respectively 0.153 mAh and 1.3602 mAh for the Graphite/Li metal coin half-cell based on aged electrode (B). They are respectively 0.202 mAh and 1.4752 mAh for the other one (C). In fact, even by applying a low charge C-rate, it appears very difficult to delithiate this aged electrode, which nevertheless remains lithiated as described above. Moreover, by applying a low discharge C-rate thereafter, it is difficult to insert more lithium into the graphite, which is certainly fully lithiated. It should be noted that lithium de/re-intercalation mechanisms into aged graphite particles are not totally obstructed since a part of Li, about 0.9 mAh, is recovered at a low rate (0.1 C) as seen in Figure 6 with Graphite/Li metal half coin cells based on harvested graphite materials. Indeed, this capacity of about 0.9 mAh measured at 0.1 C represent about 1/3 of the capacity of the fresh graphite at the same C-rate which is about 2.8 mAh. It appears here clearly that only the negative electrode is involved in the loss of capacity.

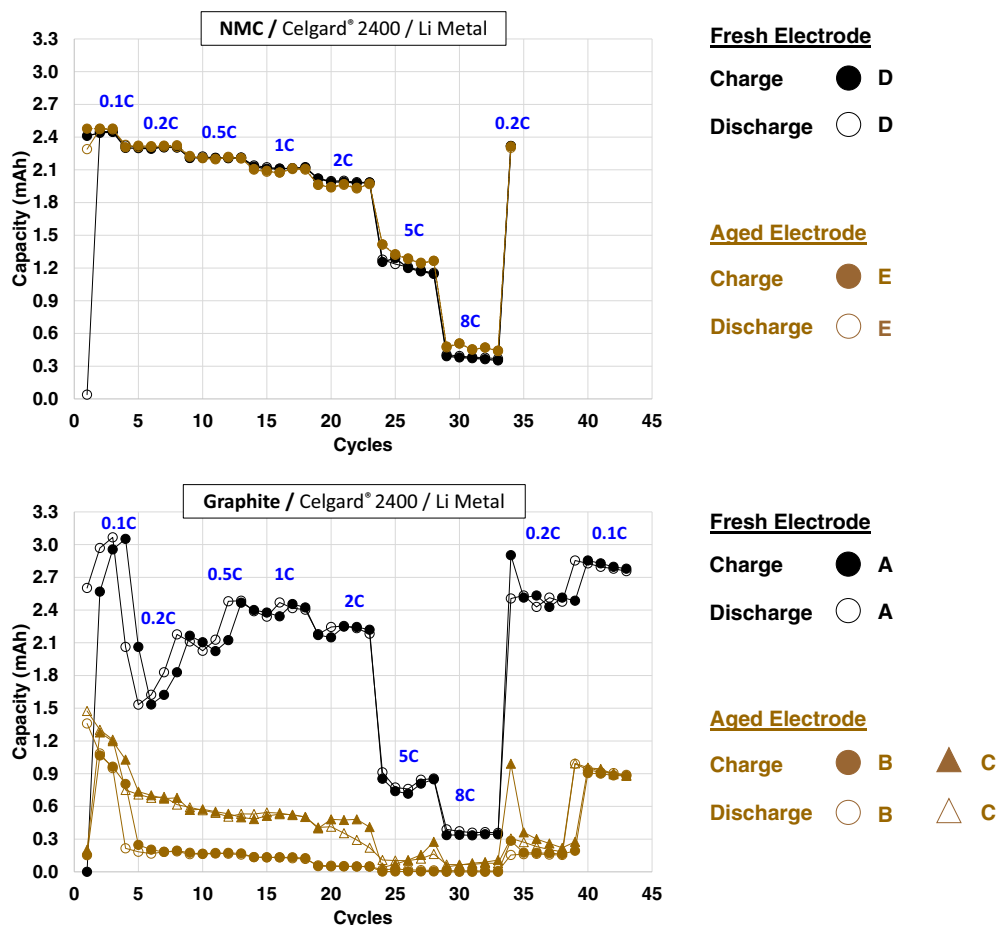


Figure 6. Electrochemical characterizations at 25°C with Graphite/Li metal and NMC/Li metal coin half-cells. No loss of capacity of insertion is observed with the NMC material recovered from the aged Li-ion cell. Lithium de/re-intercalation mechanisms are hindered with the aged graphite electrode.

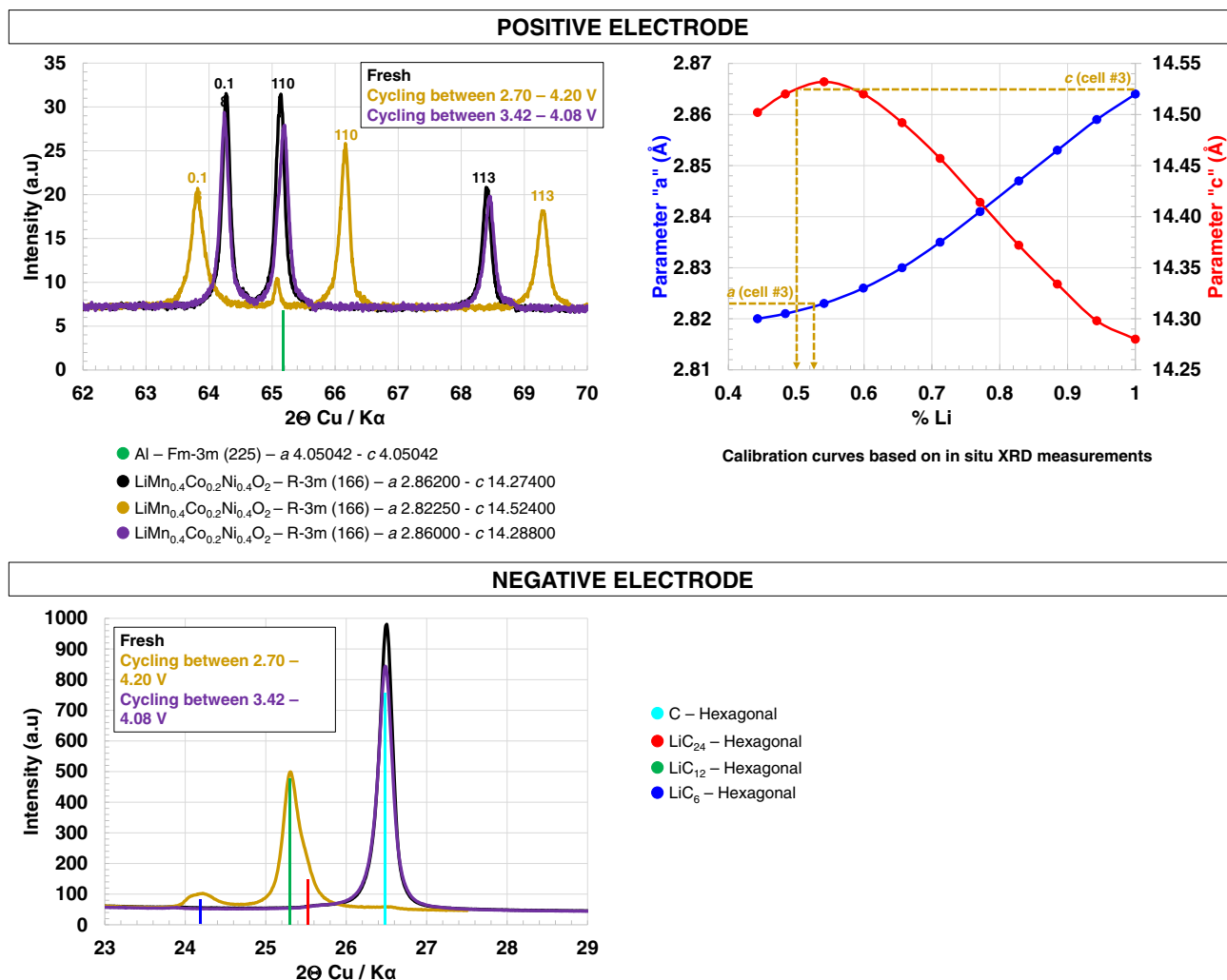


Figure 7. XRD studies of the cathode $\text{Li}_x(\text{Mn}_{0.4}\text{Co}_{0.2}\text{Ni}_{0.4})\text{O}_2$ and anode (Graphite) materials. In situ XRD measurements are performed on a sample of a fresh cathode electrode in order to obtain a calibration curve of lattice parameters in function of lithium rate.

Determination of the state of lithiation of electrodes with XRD measurements.—

XRD studies of the cathode material.—Samples of positive electrodes respectively recovered from the fresh 16 Ah Li-ion cell, from the cell #3 (dismantled after full cycling at 5°C) and from the cell #5 (dismantled after cycling at 5°C between 3.42 V – 4.08 V) are analyzed with XRD measurements. All samples possess a layered structure described in the R-3m space group for which lattice parameters a and c are calculated.

In situ XRD measurements are performed on a sample of the fresh NMC electrode. This technique is used to obtain lattice parameters of the R-3m rhombohedral phase as a function of the state of charge and the lithium content x in $\text{Li}_x(\text{Mn}_{0.37}\text{Co}_{0.22}\text{Ni}_{0.41})\text{O}_2$. This calibration curve is useful for the estimation of the lithium rate “ x ” into the aged NMC electrode based on the values of lattice parameters. In the literature, as reported by I. Buchberger⁵⁷ et al., various methods have been used to demonstrate that the lattice parameters are correlated to the lithium content of the NMC electrode (x in $\text{Li}_{1-x}\text{Ni}_{1/3}\text{Mn}_{1/3}\text{Co}_{1/3}\text{O}_2$) such as chemical or electrochemical delithiation combined with Inductively Coupled Plasma, XRD, Neutron Diffraction, or combinations of these methods. But to quantify the Li-loss, an in situ XRD calibration curve is suitable to correlate the transferred electrochemical charge to the Li content of NMC and its lattice parameters. This can be obtained using in situ XRD during charging and discharging of NMC electrode.⁵⁷

Figure 7 illustrates XRD measurements performed on positive electrodes (left figure) and the calibration curve obtained from in situ measurements with a fresh NMC sample (right figure). The left figure presents the contribution of $K\alpha_1$ of the reflections 018, 110 and 113 for the fresh and cycled samples. The Aluminum collector peaks are visible. Lattice parameters obtained from the NMC recovered from the cell #5 are equal to those determined from the fresh cathode while those obtained with the NMC electrode recovered from the cell #3 have significantly evolved.

The NMC samples respectively recovered from the fresh cell and the cell #5 present the expected lithiated state while the cathode from the most degraded cell is highly delithiated. We hypothesize that the rate of lithium $x = 1$ for the fresh material failing to dispose of a sample of pristine commercial cathode material. Note that the value of the a parameter has decreased from 2.862 Å (fresh - lithiated) to 2.823 Å (aged - delithiated) and that of the c parameter has increased from 14.274 Å (fresh - lithiated) to 14.524 Å (aged - delithiated). This reflects a delithiated state in the structure of the cathode material recovered from the cell #3. The decrease of a and the increase of c with delithiation are in good agreement with the observations of S.-C. Yin et al. using Neutron Diffraction studies on $\text{Li}_{1-x}\text{Ni}_{1/3}\text{Mn}_{1/3}\text{Co}_{1/3}\text{O}_2$ samples.⁵⁸ J. Choi et al.⁵⁹ further investigated in the variations of the lattice parameters with lithium content ($1-x$) in $\text{Li}_{1-x}\text{Ni}_{1/3}\text{Mn}_{1/3}\text{Co}_{1/3}\text{O}_2$ using XRD measurements. They reported that the c parameter increases initially with decreasing lithium content due

Table V. Content (%) of each component of the electrolyte detected with GC-MS analysis performed on samples recovered from a fresh cell and from cell #3.

	Content (%) of each component	
	Fresh	cyc@5°C
Solvents		
EMC	53.52	23.65
EC	32.53	24.05
Additives		
VC	0.10	0
FEC	0.88	0.15
Biphenyl	10.57	10.57
1,3-PS	2.40	0.52
Decomposition products		
DMC	0	3.34
DEC	0	17.04
EGMC	0	0.79
2-ethoxycarbonyloxyethyl methyl carbonate	0	2.30
DEDOHC	0	1.77
TOTAL	100	84.18
Gas and/or not detected material	0	15.82

to an increasing electrostatic repulsion across the Van der Waals gap between the (Ni_{1/3}Mn_{1/3}Co_{1/3}) O₂ sheets.

As suggested by several authors,^{60–62} it is also possible to calculate the lithium content into a NMC sample by reporting the corresponding values of lattice parameters on the calibration curves determined with the fresh NMC in situ XRD measurements. This technique confirms that the NMC electrode recovered from the aged cell is delithiated although the cell was disassembled in discharged state.

XRD studies of the anode material.—XRD measurements have been conducted on graphite samples respectively recovered from the fresh cell, the cell #3 and the cell #5. Figure 7 presents XRD measurements performed on negative electrodes. Signals corresponding respectively to the graphite electrode recovered from the cell #5 and from the fresh cell have the same signature.

The relative intensity of the hexagonal graphite peaks have decreased for the most aged material (cell #3) compared to the fresh material. Nevertheless, what is astounding is the concurrent presence of intercalation compounds (LiC₆, LiC₁₂ and LiC₂₄) found into the aged graphite. This result reveals that a considerable part of exchangeable lithium was trapped as graphite intercalation compounds. It is consistent with the brown color on the surface of graphite electrode as shown in Figure 4. This also highlights that it has not been possible to more lithiate the graphite during coin half-cells electrochemical measurements. However, it remains to determine why it is no longer possible to delithiate this electrode. It may be assumed that there could be a correlation between a probably thick layer formed on the surface and between graphite particles and the loss of its capacity of de/re-intercalation.

Influence of the electrolyte.—*Electrolyte analysis with GC-MS.*—

In order to follow the evolution of each component with aging, GC-MS analyses are performed on a sample of the electrolyte recovered from a fresh commercial Li-ion cell and on a sample recovered from the cell #3. Original electrolyte components of the commercial pouch cell¹⁰ can be identified from the fresh electrolyte analysis as following: solvents (ethyl methyl carbonate (EMC) and ethylene carbonate (EC)) and many additives (vinylene carbonate (VC), fluoroethylene carbonate (FEC), biphenyl (BP) and 1,3-propane sultone (PS)).

Table V illustrates the content of each detected element. The analysis of the electrolyte retrieved from the cell #3 reveals the presence of additional components identified as electrolyte decomposition products: dimethyl carbonate (DMC), diethyl carbonate (DEC), ethyleneg-

Table VI. The average of capacity loss (after 50 cycles) of coin full cells per type of electrolyte is based on charged capacities measured during check-up at 25°C (before and after cycling) respectively at a rate of 0.1C, 0.2C, 0.5C and 1C.

Electrolyte	Loss of capacity (%)			
	0.1 C	0.2 C	0.5 C	1 C
1	57	54	54	50
2	52	47	46	43
3	47	40	43	38
4	31	29	22	20
5	38	38	38	34
6	49	48	47	45

lycol bis-(methyl carbonate) (EGMC), 2-ethoxycarbonyloxyethyl methyl carbonate and diethyl 2,5-dioxane dicarboxylate (DEDOHC).

The content of solvents has decreased significantly at 5°C and VC additive is totally consumed with aging. FEC and 1,3-PS show lower concentrations. In any case, the degradation of solvents content and the apparition of many electrolyte degradation products during cycling is clearly identified.

The organic electrolytes used in lithium-ion batteries have oxidation potentials around 4.7 V vs. Li⁺/Li and reduction potentials close to 1.0 V vs. Li⁺/Li. But, the intercalation potential of Li into graphite is between 0.05 V and 0.1 V vs. Li⁺/Li, which is below the reduction potential of the electrolyte. As mentioned in the Introduction, charging at low temperatures increases internal resistance which can lower the potential of graphite below 0 V vs. Li⁺/Li, hence lithium metal deposition on the anode is facilitated. As a result, the potential of the graphite electrodes falls below the stability window of the electrolyte during charging, and it leads to the decomposition of the electrolyte at the graphite surface forming a passivation layer.

Influence of the composition of the electrolyte.—The investigation consists in testing electrolytes of different chemical composition with coin full cells based on electrodes recovered from a fresh 16 Ah commercial Li-ion cell. Electrolytes are synthesized based on components detected from a fresh electrolyte with GC-MS as shown in Table V. Li-ion coin full cells are cycled at 5°C between 2.7–4.2 V. As with 16 Ah commercial pouch-cells, a check-up is performed at 25°C before and after cycling for measuring the capacity loss. The aim is to identify the impact of each element of the electrolyte on the fast loss of performance. All the six synthesized electrolytes are presented in Table III. The electrolyte #1 corresponds to the original composition of the fresh commercial electrolyte. For the others compositions, an additive is removed successively in order to study the influence on cycling performance. The electrolyte #6 does not retain any additives. Only dimethyl carbonate is added as solvent in order to obtain a standard electrolyte.

The same signature of a fast decrease of performance in only 50 cycles, already observed with commercial cells as seen in Figure 2, is also put into evidence here with the all coin full cells. The average of capacity loss per type of electrolyte based on charged capacities measured at different C-rates during the check-up is presented in Table VI. A fast performance fade is observed whatever the nature of the electrolyte.

Figure 8 illustrates visual inspections of components of those coin full cells based on different composition of electrolyte after cycling at 5°C. Coin full cells are disassembled at a discharged state after a discharge applied at rate of 0.1C (see Experimental section). It is remarkable to observe that there is no interesting defect on the positive electrode and on the separator which remained white. In addition, the graphite remained lithiated regardless the composition of the electrolyte for the all coin full cells. This mechanism is therefore reproducible as with 16 Ah commercial Li-ion cells than with coin full cells. Areas that have not been in contact with the opposite electrode remained in black color. No metallic lithium is visually observed. This







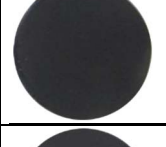


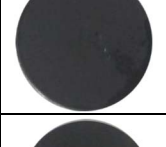

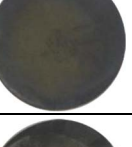






Electrolytes		NMC	Separator	Graphite
E1				
EC+EMC+ LiPF ₆ 1M	BP+PS+FEC+VC			
E2				
EC+EMC+ LiPF ₆ 1M	BP+PS+FEC			
E3				
EC+EMC+ LiPF ₆ 1M	BP+PS			
E4				
EC+EMC+ LiPF ₆ 1M	BP			
E5				
EC+EMC+ LiPF ₆ 1M	PS			
E6				
EC+EMC+DMC+ LiPF ₆ 1M				

Figure 8. Visual inspections of components of coin full cells after cycling at 5°C.

result demonstrates that there is no notable influence of the nature of the electrolyte in this aging mechanism. It is therefore the graphite electrode that would be involved.

Influence of passivation films on graphite electrodes.—Detection of metallic lithium with ⁷Li NMR.—⁷Li NMR under fast magic angle spinning appears to be useful for ex situ and post-mortem analyses of battery electrodes. Figure 9 illustrates ⁷Li NMR measurements performed on graphite electrodes retrieved respectively from the cell

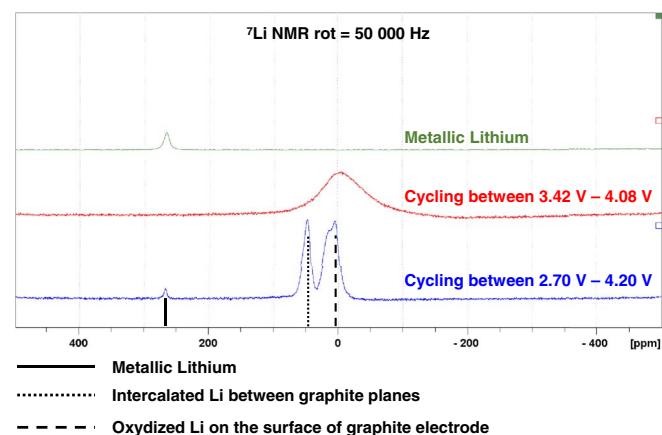


Figure 9. ⁷Li NMR analysis: Metallic lithium detection on graphite electrode recovered from the cell #3.

#3 and the cell #5. The presence of metallic lithium is detected with a lower intensity only on the most degraded anode with a specific signal centered at 260 ppm. The high signal at 0 ppm is assigned to lithium in diamagnetic compound complexes with graphite derivatives for instance or diamagnetic inorganic salts indicating the presence of the SEI.¹⁰ There is an additional high intensity peak at 50 ppm, corresponding to intercalated Li between graphite planes. W.-C. Oh⁶³ reported that a Knight shift of 44.32 ppm corresponding to the LiC₆ compound indicates an electrical field gradient at the lithium nucleus site with a quasiaxial symmetry.

It is quite possible that lithium plating formed during cycling has been stripped from graphite electrodes, since the cell has been opened at discharged state. This would mean a part of plated lithium is reversible. However, this assumption is not consistent with the irreversible loss of capacity which is about 75% based on measurements at 25°C (see in Table I). It may be assumed that metallic lithium depositions formed during cycling as well as the lithium present in the form of graphite intercalation compounds are hindered by a layer constituted by electrolyte degradation products. Whatever, it appears here that lithium remains in large amounts trapped into graphite electrode obstructed by a layer composed of electrolyte degradation products.

Chemical investigation into the volume of graphite electrodes with FIB/ToF-SIMS.—Figure 10 presents normalized elemental mappings of graphite electrodes recovered from the cell #3 and from the cell #5. For the cell #5 (cycling between 3.42 V and 4.08 V), lithium signal is weak and presents almost no contrast, confirming the near absence of lithium. Fluorine is mainly detected at the surface of the electrode (left part of the image – outlined in red) which indicates the presence of

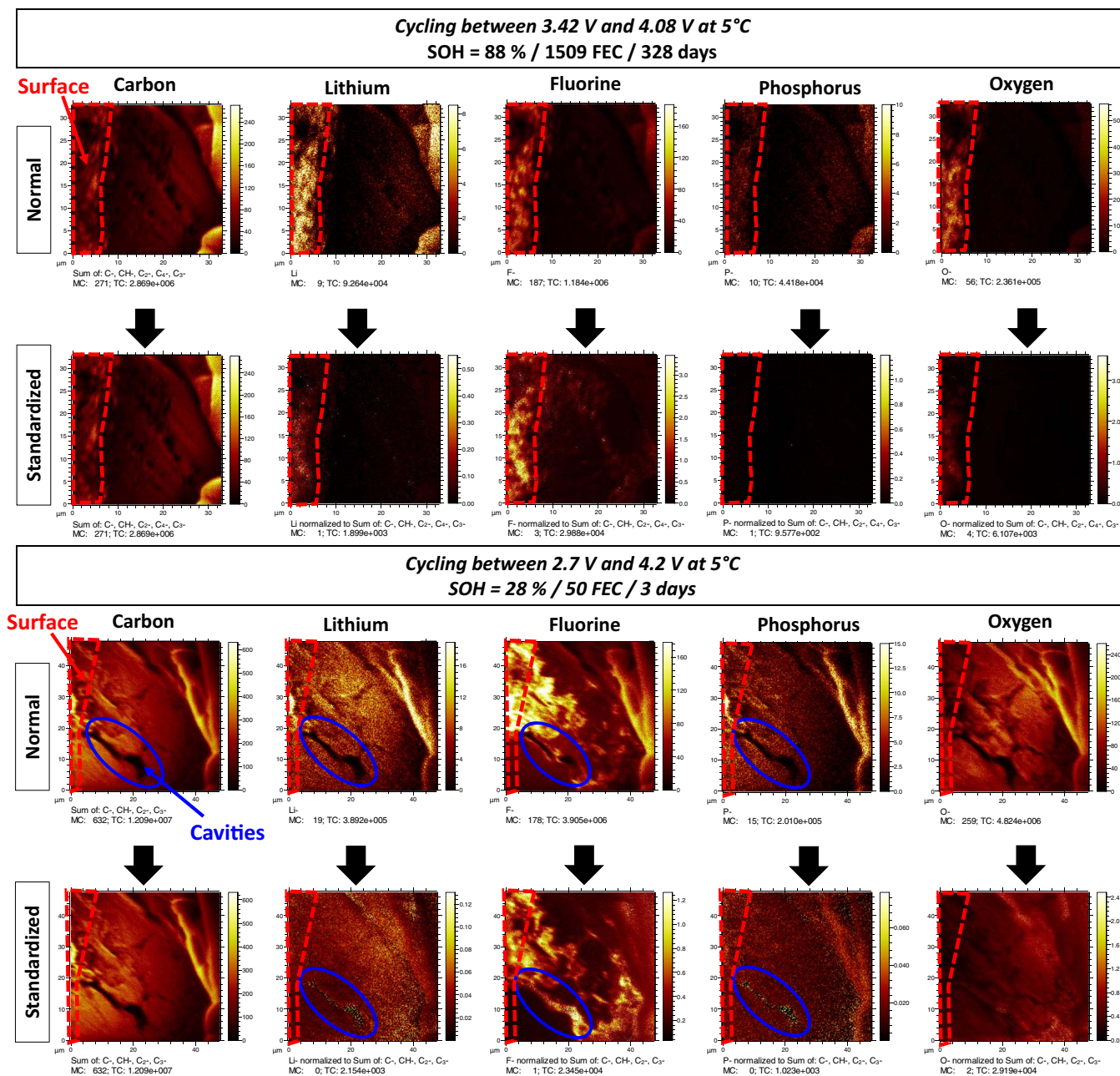


Figure 10. ToF-SIMS images: Standardization of the rate of each characteristic element in function of the graphite “carbon” rate. No significant changes with standardization is observed with the graphite recovered from the cell #5 (cycling between 3.42 V and 4.08 V). Lithium is trapped, seen enriched in inter-particles cavities of the graphite electrode recovered from cell #3 (cycling between 2.7 V and 4.2 V). In blue circular areas, the Li / C ratio and P / C ratio are more important.

SEI, and also slightly around graphite grains. For the cell #3 (cycling between 2.7 V and 4.2 V), fluorine mapping is different: the observed contrast is representative of a higher concentration in the regions corresponding to the cavities between or within particles. This is an indication that in that case, the inter-particles cavities are filled with SEI. Moreover, lithium mapping presents a signal contrast fitting the graphite particles mapping (see carbon mapping), confirming lithium trapping into the graphite particles.

Chemical investigation of passivation films on graphite electrodes with XPS.—We aim to further investigate on graphite electrodes recovered from the cell #3 and cell #5 which were subjected to FIB-SIMS analyses suggesting SEI compounds in significant quantities into the electrode porosity. In the literature, it is reported that the elevated temperatures accelerate the formation of passivation films on anode.⁴⁰

The growth of the SEI was found to be rather favored by high state of charge and high temperature storage conditions.^{12–14} In the case of this study, it would be unlikely to suggest a growth of the regular SEI favored at 5°C. In contrast to the typical nanometer SEI film reported in the literature, the formation of an untypical layer composed of electrolyte decomposition products obstructing the graphite electrode pores and then de/re-lithiation mechanisms seems to be more appropriate.

The objective of XPS is to compare the chemical composition of the passivation films at the surface of both graphite electrodes. Figure 11 presents the XPS spectroscopic analysis results for both graphite electrodes.

Spectroscopic analysis.—

C 1s analysis.—The C 1s spectrum of graphite from the cell #5 presents one asymmetric peak, whose maximum is at 284.6 eV. This

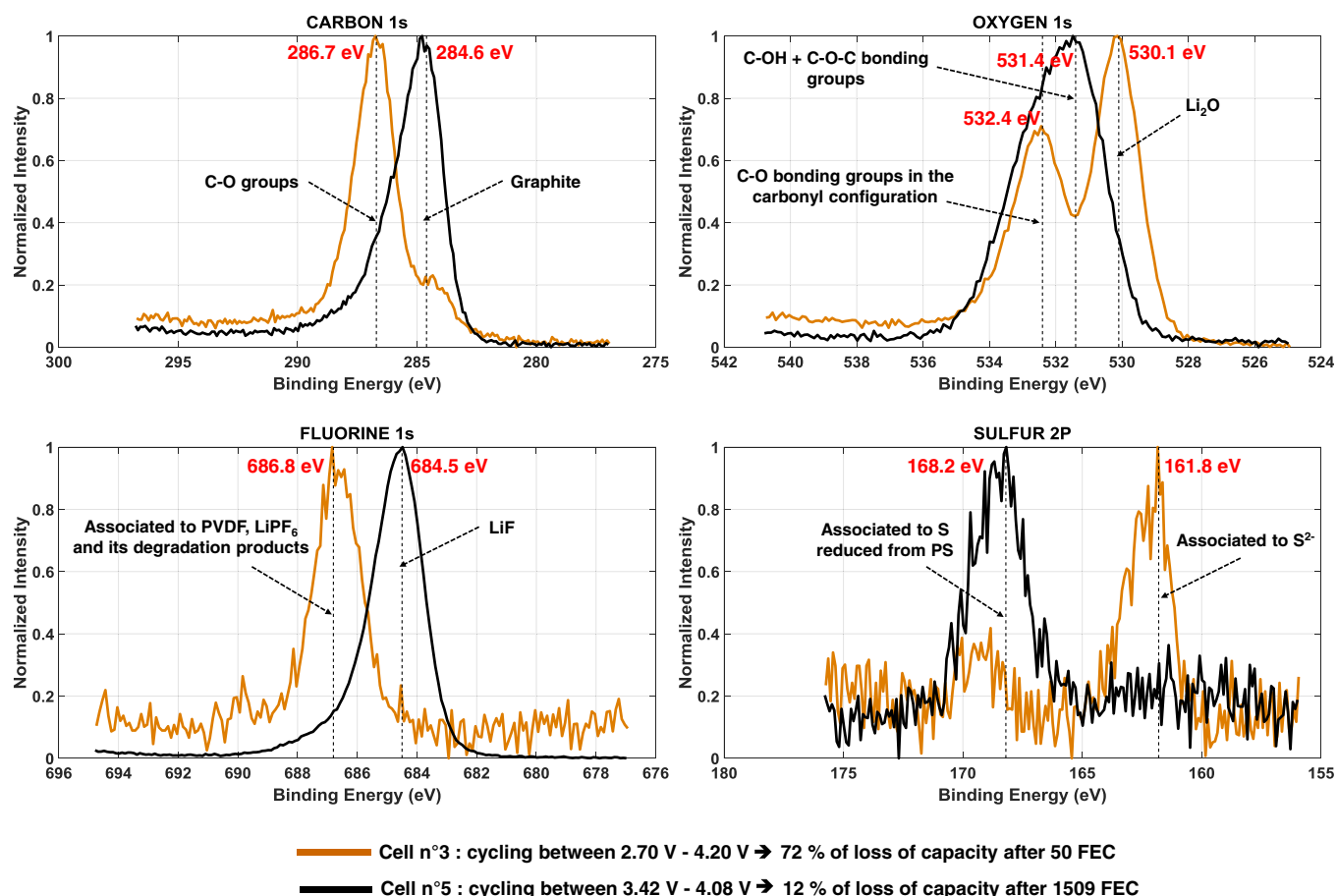


Figure 11. Spectroscopic analysis of graphite electrodes with XPS technique.

peak can be related to the presence of the active material (graphite particles) probably mixed with carbon black.^{64,65} Its relative high intensity confirms that the passivation layer is thin (regular SEI), probably no more than 2 or 3 nm. In contrast, the C 1s XPS spectrum of graphite from the cell #3 presents one main peak at 286.7 eV associated to C-O groups, and a tiny shoulder of lower intensity at 284.6 eV. This is a clear indication of the presence of a thicker layer screening the photoelectrons originated from the graphite particles. It can be assumed that this thick layer is composed of the expected SEI and the accumulation of electrolyte degradation products impeding carbon pores.

F 1s analysis.— The F 1s spectra of both electrodes show 2 peaks located at different binding energies. The sample from the cell #5 presents one intense peak at 684.5 eV which can be explained by the presence of LiF^{65,66} compounds while the surface of the electrode #3 is characterized by a peak of lower intensity at the same binding energy. This could indicate the absence of the LiF compounds in the composition of the regular SEI formed on the graphite surface. Nevertheless, this hypothesis remains unlikely. The most likely explanation is that the presence of a layer formed over the LiF compounds, suspected to hinder graphite electrode pores, is shielding the photoelectrons originated from these lithium fluoride compounds as it has been observed with carbon particles. Besides, this graphite electrode shows one intense peak at 686.8 eV, which may be associated to PVDF, LiPF₆ and its degradation products such as lithium phosphofluorides.⁶⁵ This observation is in agreement with GC-MS results: the degradation of solvents had led to the apparition of many electrolyte degradation products.

O 1s analysis.— The O 1s XPS spectra are quite different between both electrodes. Graphite electrode from the cell #5 presents a wide shoulder centered at a higher binding energy (531.4 eV): this is typical of SEI with a wide range of oxidized species and C-OH and/or C-O-C bonds.^{65,67,68} Graphite electrode from the cell #3 presents two well separated peaks. The lower binding energy peak (530.1 eV) is associated with Li₂O,^{65,69} while the other one (532.4 eV) corresponds to C-O bonding groups in the carbonyl group or lithium carbonate molecule.⁶⁶

S 2p analysis.— The peak associated to the sample retrieved from the cell #5 is located at a higher binding energy of 168.2 eV, which is typical of S reduced from 1,3 propane sultone.⁶⁷ Surprisingly, the S 2p of the graphite electrode from the cell #3 presents a lower binding energy peak (161.8 eV), which is assigned to S²⁻.⁶⁷

The respective passivation films chemical compositions are given in Table VII. Graphite electrode recovered from the cell #5 presents a Li/F ratio close to 1, relative to the high presence of amounts of

Table VII. Percentage of each element detected with XPS on the surface of samples of graphite electrodes respectively recovered from the cell #3 (cycling between 2.70 V and 4.20 V) and from the cell #5 (cycling 3.42 V and 4.08 V).

Element	C	O	F	P	S	Li
% at. Cell #3	24.7	19.3	1.8	0	0.5	53.7
Cell #5	24.1	10.5	32.7	2	0.5	30.3

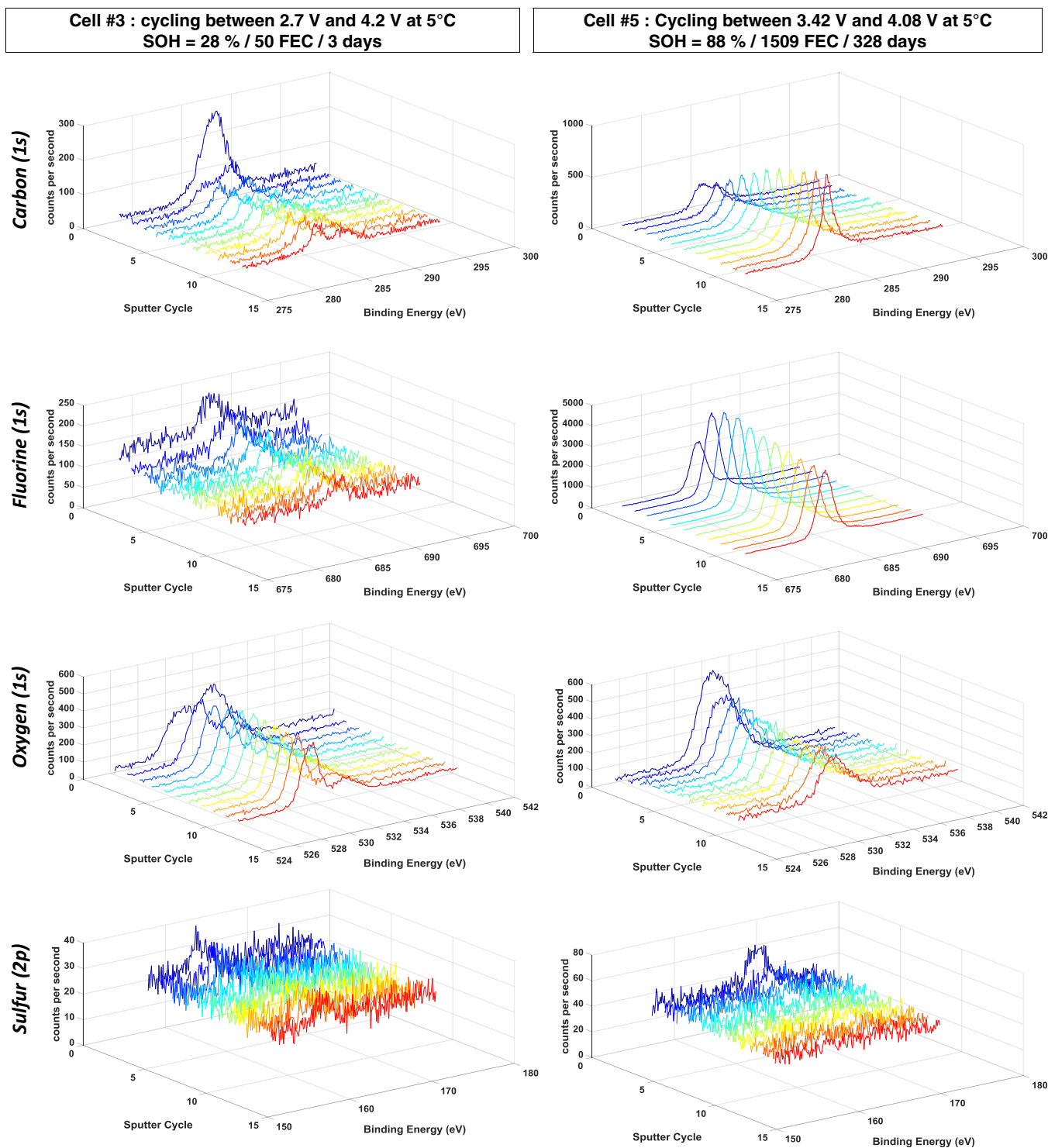


Figure 12. Profilmetric analysis graphite electrodes with XPS technique.

LiF (confirmed by F 1s spectra). Other elements (C, O, and P) are probably related to the presence of (poly(ethylene oxide)) PEO-type oligomers, ROCO_2Li and $\text{Li}_x\text{PO}_y\text{F}_z$ compounds. On the contrary, the composition of the electrode of the cell #3 presents high amounts of Li and a very high Li/F ratio, which relativizes on the low presence of LiF. R. Castaing et al. reported that LiF may be dissolved in the electrolyte instead of being deposited at the surface of active material grains.⁷⁰ It is here probably screened by another layer based on accumulation of electrolyte degradation products constituting an additional layer over

LiF or modified by reacting with these compounds as confirmed by XPS F 1s spectrum which validates the presence of Li_xPF_y species instead. This can be explained by the presence of Li_2O . Note that ToF-SIMS analysis showed that inter-particles cavities were filled with fluorine. C. Marxer et al.⁷¹ reported that ToF-SIMS analysis is more sensitive than the XPS, particularly for the detection of fluorine, for which the yield is very high.

Figure 12 presents XPS profilmetric analyses of the surface of both graphite electrodes.

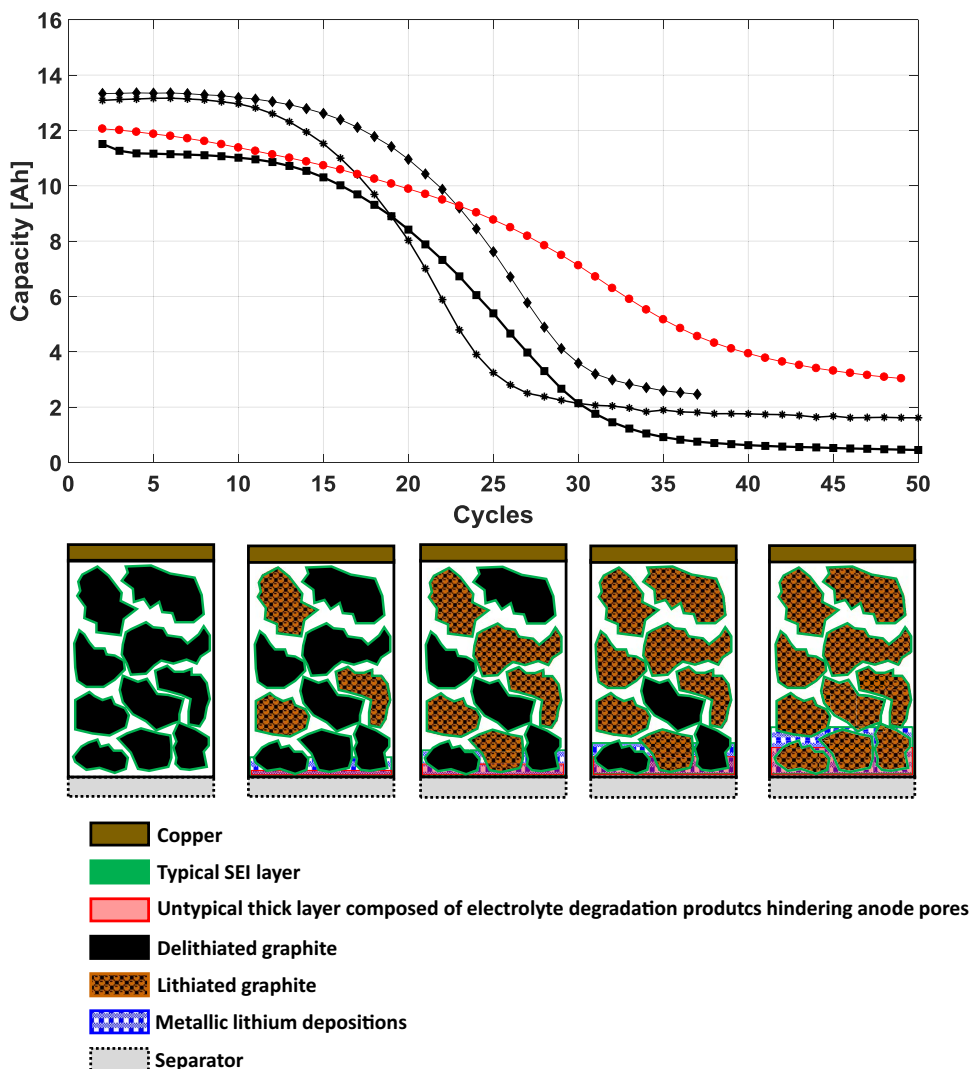


Figure 13. Representation of the mechanism leading to the hindrance of Li diffusion into graphite electrode, observed during cycling at 5°C between 2.7 V and 4.2 V.

Profilometric analysis.—

C 1s analysis.— C 1s profile concentration shows the extinction of the peak at higher binding energy (286.7 eV) after the first sputtering step, confirming the thinness of the layer formed by C-O species on the surface of the remained lithiated graphite electrode (cell #3). After the first sputtering step, the intensity of the carbon peak becomes constant. It can be said that this peak then corresponds to the carbon of the active material. The concentration profile for the graphite electrode of the cell #5 is quite different. The peak corresponding to the graphite contribution increases with the number of sputter cycles.

F 1s analysis.— F 1s profiling concentrations show that LiF is not present even in the internal part of the SEI, in the case of electrode of the cell #3: it has probably been degraded with cycling or it may be assumed that it had reacted with other degradation products. Otherwise for the other electrode (cell #5), LiF remains present throughout the SEI.

O 1s analysis.— On one hand, the O 1s XPS profiling concentrations show a decrease of the peak corresponding to species identified as C-O bonding groups at 532.4 eV for the aged graphite (cell #3). On the other hand, a decrease of the wide shoulder centered at 531.4 eV is also observed for the non-degraded graphite (cell #5).

S 2p analysis.— For the non-degraded graphite (cell #5), the peak observed at ~168.2 eV disappears after the first sputtering step: this suggests that this contribution is linked to some traces of the electrolyte

deposition at the surface which are quickly removed with sputtering. On the contrary, for the aged graphite, the numerous sputtering steps do not remove the peak observed at 161.8 eV which remains until the end of the profile. This strongly suggests that this peak is due to the presence of a degraded (reduced) product of PS in the whole depth of the SEI.

Representation of the mechanism leading to the hindrance of Li diffusion into graphite electrode.—

Figure 13 presents a scheme that explains the formation of an untypical layer constituted by electrolyte degradation products, occurring during cycling of 16 Ah commercial Li-ion cells at 5°C between 2.7 V and 4.2 V. This scheme is inspired by the schematic illustration of the aging behavior of a cell undergoing cycling with transition from linear to nonlinear aging as proposed by X.-G. Yang et al.⁷² In that paper, the authors presented a physics-based Li-ion battery aging model accounting for both lithium plating and solid electrolyte interphase (SEI) growth.

The evolution of the state of the graphite electrode is represented in Figure 13 at the end of discharge as the number of cycles increases. During cycling the regular SEI layer as reported in the literature^{12–14,40} does not grow since its growth is rather favored by high temperature and high state of charge.

Besides, charging at low temperatures increases internal resistance which can lower the potential of graphite below 0 V vs. Li⁺/Li. As a

result, the potential of the graphite electrodes falls below the stability window of the electrolyte during charging. On one hand, it leads to the decomposition of the solvents of the electrolyte forming a specific layer on top of and within the graphite electrode. Note that the analysis of the electrolyte show a strong degradation of solvents and the apparition of many degradation products (see in Table V). On the other hand, local metallic lithium depositions are facilitated.

As the number of cycles increases, this untypical layer grows and hinders more and more the pores of the graphite electrode so that de/re-intercalation mechanisms are then significantly reduced. Consequently, some areas of the graphite electrode remain lithiated. It is then more and more difficult to extract lithium cations from graphite particles in order to intercalate into the positive electrode as well with the evolution of the end-of-charge/discharge potentials of both electrodes pointed out in Figure 3. Therefore, this mechanism leads to an irreversible capacity loss of about 75% in only 50 cycles as illustrated in Figure 2 and in Table I. Moreover, visual inspections in Figure 4 show that graphite electrodes remain unexpectedly lithiated although the cell was dismantled after a discharge performed twice at rate of 0.1 C. The positive electrode was therefore not fully lithiated during the last discharge before dismantling.

Metallic lithium depositions have grown in height since lithium dendrites are distinguished with SEM images (see in Figure 5) on the surface of the graphite electrode. These deposits are detected in small amounts with ^7Li NMR analysis (see in Figure 9) while peaks of high intensity respectively assigned to Li in diamagnetic compound complexes and intercalated Li between graphite planes are notable.

The chemical composition on the surface of the aged graphite electrode with XPS shows that this untypical layer is composed of C-O bonding species; Li_2O ; lithium carbonates; PVDF, LiPF_6 and its degradation products ($\text{Li}_x\text{PO}_y\text{F}_z$ compounds).

Conclusions

A fast loss of performance around 75% was observed during fully cycling at 5°C (after only 50 cycles). Graphite electrodes of 16 Ah commercial Li-ion cells remained unexpectedly lithiated after dismantling at a discharged state. Electrochemical measurements with full coin cells demonstrated that there is no influence of the nature of the electrolyte in the aging mechanism. The evolution of the end-of-charge/discharge potentials of both electrodes during cycling obtained from the Li-ion cell instrumented with reference electrode showed difficulties to extract more lithium cations from graphite to intercalate to the positive electrode, which exhibited then after a good cycling performance in NMC/Li Metal half coin cells.

The analysis of the electrolyte with GC-MS showed a strong solvents decomposition and the apparition of many degradation products which have accumulated in the pores of graphite electrodes during cycling to form an untypical layer hindering Li-ions diffusion pathways in the anode. Consequently, some areas of the graphite electrode remain lithiated since de/re-intercalation mechanisms are significantly reduced into the negative electrodes. As a result, lithium inventory decreases strongly at each cycle and cell fails rapidly.

Based on XPS results, it can be assumed that this thick layer impeding the electrode porosity is mainly formed by C-O bonding species; Li_2O ; lithium carbonates; PVDF, LiPF_6 and its degradation products ($\text{Li}_x\text{PO}_y\text{F}_z$ compounds). A low intensity peak indicating metallic lithium is detected with ^7Li NMR analysis. It may be accepted that lithium plating formed during cycling could be stripped from graphite electrodes considering the cell has been disassembled at discharged state. However, lithium dendrites are well distinguished on the surface of the remained lithiated graphite with SEM images.

The fact that graphite remained lithiated may be explained by the hindrance of the electrode porosity, preventing diffusion of the remaining cyclable lithium into the electrode depth. Moreover, the higher reduction level imposed by the cycling conditions may induce a drastic degradation of the electrolyte. These results are consistent with the interpretation in FIB-SIMS which suggests the obstructing of the porosity of the graphite electrode.

References

- J. Vetter, P. Novák, M. R. Wagner, C. Veit, K.-C. Möller, J. O. Besenhard, M. Winter, M. Wohlfahrt-Mehrens, C. Vogler, and A. Hammouche, "Ageing mechanisms in lithium-ion batteries," *J. Power Sources*, **145**, 269 (2005).
- M. Gauthier, T. J. Carney, A. Grimaud, L. Giordano, N. Pour, H.-H. Chang, D. P. Fenning, S. F. Lux, O. Paschos, C. Bauer, F. Maglia, S. Lupat, P. Lamp, and Y. Shao-Horn, "Electrode-Electrolyte Interface in Li-ion Batteries: Current Understanding and New Insights," *J. Phys. Chem. Lett.*, **6**, 4653 (2015).
- W. A. van Schalkwijk and B. Scrosati, *Advances in lithium-ion batteries*, Klumer Academics Publishers, 155–181.
- D. Takamatsu, Y. Orikasa, S. Mori, T. Nakatsutsumi, K. Yamamoto, Y. Koyama, T. Minato, T. Hirano, H. Tanida, H. Arai, Y. Uchimoto, and Z. Ogumi, "Effect of an electrolyte additive of vinylene carbonate on the electronic structure at the surface of a lithium cobalt oxide electrode under battery operating conditions," *J. Phys. Chem. C*, **119**, 9791–9797 (2015).
- E. Markevich, G. Salitra, K. Fridman, R. Sharabi, G. Gershenko, A. Garsuch, G. Semrau, M. A. Schimdt, and D. Aurbach, "Fluoroethylene carbonate as important component in electrolyte solutions for high-voltage lithium batteries: role of surface chemistry on the cathode," *Langmuir*, **30**(25), 7414 (2014).
- Y. Ein-Eli, "Dimethyl carbonates (DMC) electrolytes - the effect of solvent purity on Li-ion intercalation into graphite anodes," *Electrochemistry communications*, **4**, 644 (2002).
- B. Zhang, M. Metzger, S. Solchenbach, M. Payne, S. Meini, H. A. Gasteiger, A. Garsuch, and B. L. Lucht, "Role of 1,3-propane sultone and vinylene carbonate in solid electrolyte interface formation and gas generation," *J. Phys. Chem. C*, **119**, 11337 (2015).
- T. R. Jow, K. Xu, O. Borodin, and M. Ue, "Electrolytes for lithium and lithium-ion batteries," *Johnson Matthey Technol. Rev.*, **59**(1), 30 (2015).
- R. Imnhof and P. Novák, "Oxydative electrolyte solvent degradation in lithium-ion batteries: an in situ differential electrochemical mass spectrometry investigation," *J. Electrochem. Soc.*, **146**(5), 1702 (1999).
- B. Pilipili Matadi, S. Geniès, A. Delaille, T. Waldmann, M. Kasper, M. Wohlfahrt-Mehrens, F. Aguesse, E. Bekaert, I. Jiménez-Gordon, L. Daniel, X. Fleury, M. Bardet, J.-F. Martin, and Y. Bultel, "Effects of Biphenyl polymerization on lithium deposition in commercial Graphite/NMC lithium-ion pouch-cells during calendar aging at high temperature," *J. Electrochem. Soc.*, **164**(6), A1089 (2017).
- P. Niehoff, E. Kraemer, and M. Winter, "Parametrisation of the influence of different cycling conditions on the capacity fade and the internal resistance increase for lithium nickel manganese cobalt oxide/graphite cells," *J. Electroanal. Chem.*, **707**, 110 (2013).
- K. Amine, J. Liu, and I. Belharouk, "High-temperature storage and cycling of C-LiFePO₄/graphite Li-ion cells," *Electrochemistry communications*, **7**, 669 (2005).
- S. Grolleau, A. Delaille, H. Gaulous, P. Gyan, R. Revel, J. Bernard, E. Redondo-Iglesias, and J. Peter, "On behalf of the SIMACL Network, Calendar aging of commercial graphite/LFP cell - Predicting capacity fade under time dependent storage conditions," *J. Power Sources*, **225**, 450 (2014).
- S. Käbitz, J. B. Gerschler, M. Ecker, Y. Yurdagel, B. Emmemacher, D. André, T. Mitsch, and D. Uwe Sauer, "Cycle and calendar life study of a graphite|LiNi_{1/3}Mn_{1/3}Co_{1/3}O₂ Li-ion high energy system. Part A: Full cell characterization," *J. Power Sources*, **239**, 572 (2013).
- M. C. Smart, B. V. Ratnakumar, and S. Surampudi, "Electrolytes for Low-Temperature Lithium Batteries Based on Ternary Mixtures of Aliphatic Carbonates," *J. Electrochem. Soc.*, **146**, 486 (1999).
- C.-K. Huang, J. S. Sakamoto, J. Wolfenstine, and S. Surampudi, "The Limits of Low-Temperature Performance of Li-Ion Cells," *J. Electrochem. Soc.*, **147**, 2893 (2000).
- V. Agubra and J. Fergus, "Lithium Ion Battery Anode Aging Mechanisms," *Materials*, **6**, 1310 (2013).
- Z. Li, J. Huang, B. Y. Liaw, V. Metzler, and J. Zhang, "A review of lithium deposition in lithium-ion and lithium metal secondary batteries," *J. Power Sources*, **254**, 184 (2014).
- Z. Guo, J. Zhu, J. Feng, and S. Du, "Direct in situ observation and explanation of lithium dendrite of commercial graphite electrodes," *RSC Adv.*, **5**, 69514 (2015).
- T. Waldmann, B.-I. Hogg, M. Kasper, S. Grolleau, C. Gutiérrez Couceiro, K. Trad, B. Pilipili Matadi, and M. Wohlfahrt-Mehrens, "Interplay of Operational Parameters on Lithium Deposition in Lithium-ion cells: Systematic Measurements with Reconstructed 3-Electrode Pouch Full Cells," *J. Electrochem. Soc.*, **163**(7), A1 (2016).
- A. Friesen, F. Horsthemke, X. Monnighoff, G. Brunklaus, R. Krafft, M. Borner, T. Risthaus, M. Winter, and F. M. Schappacher, "Impact of cycling at low temperatures on the safety behavior of 18650-type lithium ion cells: Combined study of mechanical and thermal abuse testing accompanied by post-mortem analysis," *Journal of Power Sources*, **334**, 1 (2016).
- M. Winter, "The Solid Electrolyte Interphase - The Most Important and the Least Understood Solid Electrolyte in Rechargeable Li Batteries," *Z. Phys. Chem.*, **223**, 1395 (2009).
- M. Petzl and M. A. Danzer, "Nondestructive detection, characterization, and qualification of lithium plating in commercial lithium ion batteries," *J. Power Sources*, **254**, 80 (2014).
- M. Petzl, M. Kasper, and M. A. Danzer, "Lithium plating in a commercial lithium-ion battery - A low-temperature aging study," *J. Power Sources*, **275**, 799 (2015).
- S. Schindler, M. Bauer, M. Petzl, and M. A. Danzer, "Voltage relaxation and impedance spectroscopy as in-operando methods for the detection of lithium plating

- on graphitic anodes in commercial lithium-ion cells," *J. Power Sources*, **304**, 170 (2016).
26. M. C. Smart and B. V. Ratnakumar, "Effects of electrolyte composition on lithium plating in lithium-ion cells," *J. Electrochem. Soc.*, **158**(4), A379 (2011).
 27. M. Wakihara and O. Yamamoto, *Lithium ion batteries: Fundamentals and Performance*, Kodansha (1998).
 28. H. Zheng, L. Tan, L. Zhang, Q. Qu, Z. Wan, Y. Wang, M. Shen, and H. Zheng, "Correlation between lithium deposition on graphite electrode and the capacity loss for LiFePO₄/graphite cells," *Electrochimica Acta*, **173**, 323 (2015).
 29. NASA Engineering and Safety Center Technical Report, *NASA Aerospace Flight Battery Program*, RP-08-75.
 30. L.-E. Downie, L.-J. Krause, J.-C. Burns, L.-D. Jensen, V.-L. Chevrier, and J.-R. Dahn, "In situ detection of lithium plating on graphite electrodes by electrochemical calorimetry," *J. Electrochem. Soc.*, **160**(4), A588 (2013).
 31. J.-C. Burns, D. A. Stevens, and J.-R. Dahn, "In situ detection of lithium plating using high precision coulometry," *J. Electrochem. Soc.*, **162**(6), A959 (2015).
 32. J. Cannarella and C. B. Arnold, "The effects of defects on localized plating in Lithium-ion Batteries," *J. Electrochem. Soc.*, **162**(7), A1365 (2015).
 33. T. Waldmann, A. Iturrondobeitia, M. Kasper, N. Ghanbari, F. Aguesse, E. Bekaert, L. Daniel, S. Geniès, I. Jimenez Gordon, M. W. Loble, E. De Vito, and M. Wohlfahrt-Mehrens, "Review—Post-Mortem Analysis of Aged Lithium-Ion Batteries: Disassembly Methodology and Physico-Chemical Analysis Techniques," *J. Power Sources*, **163**, A2149 (2016).
 34. S. J. Harris, A. Timmons, D. R. Baker, and C. Monroe, "Direct in situ measurements of Li transport in Li-ion battery negative electrodes," *Chemical Physics Letters*, **485**, 265 (2010).
 35. C. Uhlmann, J. Illig, M. Ender, R. Schuster, and E. Ivers-Tiffée, "In situ detection of lithium metal plating on graphite in experimental cells," *J. Power Sources*, **279**, 428 (2015).
 36. J. Steiger, D. Kramer, and R. Mönig, "Mechanisms of dendritic growth investigated by in situ light microscopy during electrodeposition and dissolution of lithium," *J. Power Sources*, **261**, 112 (2014).
 37. O. Crowther and A. C. West, "Effect of Electrolyte Composition on Lithium Dendrite Growth," *J. Electrochem. Soc.*, **155**(11), A806 (2008).
 38. H. Wu, D. Zhuo, D. Kong, and Y. Cui, "Improving battery safety by early detection of internal shorting with a bifunctional separator," *Nature Communications*, **5**, 5193 (2014).
 39. R. G. Lerner and G. L. Trigg, *Encyclopedia of physics*, VCH, New York (1991).
 40. T. Waldmann, M. Wilka, M. Kasper, M. Fleischhammer, and M. Wohlfahrt-Mehrens, "Temperature dependent ageing mechanism in lithium-ion batteries - A Post-mortem study," *J. Power Sources*, **262**, 129 (2014).
 41. H. Honbo, K. Takei, Y. Ishii, and T. Nishida, "Electrochemical properties and Li deposition morphologies of surface modified graphite after grinding," *J. Power Sources*, **189**, 337 (2009).
 42. P. Verma, P. Maire, and P. Novák, "A review of the features and analyses of the solid electrolyte interphase in Li-ion batteries," *Electrochimica Acta*, **55**, 6332 (2010).
 43. F. German, A. Hintennach, A. LaCroix, D. Thiemig, S. Oswald, F. Scheiba, M. J. Hoffmann, and H. Ehrenberg, "Influence of temperature and upper cutoff voltage on the formation of lithium-ion cells," *Journal of Power Sources*, **264**, 100 (2014).
 44. N. Ghanbari, T. Waldmann, M. Kasper, P. Axmann, and M. Wohlfahrt-Mehrens, "Detection of Li Deposition by Glow Discharge Optical Emission Spectroscopy in Post-Mortem Analysis," *ECS Electrochemistry Letters*, **4**(9), A100 (2015).
 45. H.-P. Lin, D. Chua, M. Salomon, H.-C. Shiao, M. Hendrickson, E. Plichta et al., "Low-Temperature Behavior of Li-Ion Cells," *Electrochem. Solid-State Lett.*, **4**(A71), 534 (2001).
 46. T. Waldmann, M. Kasper, and M. Wohlfahrt-Mehrens, "Optimization of Charging Strategy by Prevention of Lithium Deposition on Anodes in high-energy Lithium-ion Batteries – Electrochemical Experiments," *Electrochimica Acta*, **178**, 525 (2015).
 47. E. McTurk, C. R. Birkl, M. R. Roberts, D. A. Howey, and P. G. Bruce, "Minimally Invasive Insertion of Reference Electrodes into Commercial Lithium-Ion Pouch Cells," *ECS Electrochem. Lett.*, **4**, A145 (2015).
 48. A. Bordes, E. De Vito, C. Haon, A. Boulineau, A. Montani, and P. Marcus, "Multiscale Investigation of Silicon Anode Li Insertion Mechanisms by Time-of-Flight Secondary Ion Mass Spectrometry Imaging Performed on an In Situ Focused Ion Beam Cross Section," *Chem. Mater.*, **28**(5), 1566 (2016).
 49. J. Fan and S. Tan, "Studies on Charging Lithium-Ion Cells at Low Temperatures," *Journal of The Electrochemical Society*, **153**(6), A1081 (2006).
 50. V. Zinth, C. Von Lüders, M. Hofmann, J. Hattendorff, I. Buchberger, S. Erhard, J. Rebelo-Kornmeier, A. Jossen, and Ralph Gilles, "Lithium plating in lithium-ion batteries at sub-ambient temperatures investigated by in situ neutron diffraction," *Journal of Power Sources*, **271**, 152e159 (2014).
 51. T. Waldmann and M. Wohlfahrt-Mehrens, "Effects of rest time after Li plating on safety behavior—ARC tests with commercial high-energy 18650 Li-ion cells," *Electrochimica Acta*, **230**, 454 (2017).
 52. W. Bao, J. Wan, X. Han, X. Cai, H. Zhu, D. Kim, D. Ma, Y. Xu, J. N. Munday, H. D. Drew, M. S. Fuhrer, and L. Hu, "Approaching the limits of transparency and conductivity in graphitic materials through lithium intercalation," *Nature Communications*, **5**, 4224 (2014).
 53. Y. Qi and S. J. Harris, "In Situ Observation of Strains during Lithiation of a Graphite Electrode," *J. Power Sources*, **157**, A741 (2010).
 54. C. Uhlmann, J. Illig, M. Ender, R. Schuster, and E. Ivers-Tiffée, "In situ detection of lithium metal plating on graphite in experimental cells," *J. Power Sources*, **259**, 428 (2015).
 55. X.-L. Wang, K. An, L. Cai, Z. Feng, S. E. Nagler, C. Daniel, K. J. Rhodes, A. D. Stoica, H. D. Skorpenske, C. Liang, W. Zhang, J. Kim, Y. Qi, and S. J. Harris, "Visualizing the chemistry and structure dynamics in lithium-ion batteries by in-situ neutron diffraction," *Scientific Reports*, **2**, 747 (2012).
 56. H. Honbo, K. Takei, Y. Ishii, and T. Nishida, "Electrochemical properties and Li deposition morphologies of surface modified graphite after grinding," *Journal of Power Sources*, **189**, 337 (2009).
 57. I. Buchberger, S. Seidlmayer, A. Pokharel, M. Piana, J. Hattendorff, P. Kudejova, R. Gilles, and H. A. Gasteiger, "Aging Analysis of Graphite/LiNi_{1/3}Mn_{1/3}Co_{1/3}O₂ Cells Using XRD, PGAA, and AC Impedance," *J. Electrochem. Soc.*, **162**(14), A2737 (2015).
 58. S.-C. Yin, Y.-H. Rho, I. Swainson, and L. F. Nazar, "X-ray/Neutron Diffraction and Electrochemical Studies of Lithium De/Re-Intercalation in Li_{1-x}Co_{1/3}Ni_{1/3}Mn_{1/3}O₂ (x = 0 → 1)," *Chem. Mater.*, **18**, 1901 (2006).
 59. J. Choi and A. Manthiram, "Role of Chemical and Structural Stabilities on the Electrochemical Properties of Layered LiNi_{1/3}Mn_{1/3}Co_{1/3}O₂ Cathodes," *J. Electrochem. Soc.*, **152**(9), A1714 (2005).
 60. D.-C. Li, T. Muta, L.-Q. Zhang, M. Yoshio, and H. Noguchi, "Effect of synthesis method on the electrochemical performance of LiNi_{1/3}Mn_{1/3}Co_{1/3}O₂ Cathodes," *J. Power Sources*, **132**, 150 (2004).
 61. N. Yabuuchi, Y. Makimura, and T. Ohzuku, "Solid-State Chemistry and Electrochemical Properties of LiCo_{1/3}Ni_{1/3}Mn_{1/3}O₂ for Advanced Lithium-Ion Batteries. III. Rechargeable Capacity and Cycleability," *J. Electrochem. Soc.*, **154**(4), A314 (2007).
 62. A. M. Rodriguez, D. Ingersoll, and D. H. Doughty, *Adv. X-Ray Anal.*, **45**, 182 (2002).
 63. W.-C. Oh, "⁷Li-NMR and Thermal Analysis for Lithium Inserted into Artificial Carbon Material," *Bull. Korean Chem. Soc.*, **22**(4) (2001).
 64. C. Xu, T. Gustadsson, K. Edström, D. Brandell, and M. Hahlin, "Interface layer formation in solid polymer electrolyte lithium batteries: an XPS study," *J. Mater. Chem. A*, **2**, 7256 (2014).
 65. R. A. Quinlan, Y.-C. Lu, D. Kwabi, Y. Shao-Horn, and A. N. Mansour, "XPS Investigation of the Electrolyte Induced Stabilization of LiCoO₂ and "AlPO₄"-Coated LiCoO₂ Composite Electrodes," *Journal of The Electrochemical Society*, **163**(2), A300 (2016).
 66. V. Eshkenazi, E. Peled, L. Burstein, and D. Golodnitsky, "XPS analysis of the SEI formed on carbonaceous materials," *Solid State Ionics*, **170**, 83 (2004).
 67. M. Lu, H. Cheng, and Y. Yang, "A comparison of solid electrolyte interphase (SEI) on the artificial graphite anode of the aged and cycled commercial lithium ion cells," *Electrochimica Acta*, **53**, 3539 (2008).
 68. H. Liu, Q. Xu, C. Yan, and Y. Qiao, "Corrosion behavior of a positive graphite electrode in vanadium redox flow battery," *Electrochimica Acta*, **56**, 8783 (2011).
 69. C. N. Taylor, J. P. Allain, B. Heim, P. S. Krstic, C. H. Skinner, and H. W. Kugel, "Surface chemistry and physics of deuterium retention in lithiated graphite," *Journal of Nuclear Materials*, **415**, S777 (2011).
 70. R. Castaing, P. Moreau, Y. Reynier, D. Schleich, S. Jouanneau Si Larbi, D. Guyomard, and N. Dupré, *Electrochimica Acta*, **155**, 391 (2015).
 71. C. G. Marxer, M. L. Kraft, P. K. Weber, I. D. Hutcheon, and S. G. Boxer, "Supported Membrane Composition Analysis by Secondary Ion Mass Spectrometry with High Lateral Resolution," *Biophysical Journal*, **88**, 2965 (2005).
 72. X.-G. Yang, Y. Leng, G. Zhang, S. Ge, and C.-Y. Wang, "Modeling of lithium plating induced aging of lithium-ion batteries: Transition from linear to nonlinear aging," *Journal of Power Sources*, **360**, 28 (2017).